



Ab-initio Many-Body Methods and Simulations with the Yambo Code | (SMR 3694)

04 Apr 2022 - 08 Apr 2022
ICTP, Trieste, Italy

P01 - ASHANI Mitonji Timothy

Electronic and Thermoelectric Properties of Half-Heusler Semiconductors $X\text{HfSn}$ ($X = \text{Ni}$ and Pt)

P02 - BABAEI BIDMESHKI Nadia

Absorption spectra for small pigment molecules: Comparing real-time TDDFT with Linear-response approach

P03 - BEZZERGA Djamel

Prediction of Large Intrinsic Ferroelectricity in Monolayer Silicon Carbide

P04 - BHAGAT Brajesh Rajesh

Intermediate band governed enhancement of photo-responsive nature for Fe-loaded and O-doped g-C₃N₄

P05 - BORGHESI Costanza

Tailoring thermal properties of High Entropy Oxides: new technologies for radiative passive cooling against global warming

P06 - CHEN Peng

Deterministic control of ferroelectric polarization by ultrafast laser pulses

P07 - COLONNA Nicola

Koopmans spectral functionals in periodic-boundary conditions

P08 - DEVI Anjna

Thermal Stability of NbX_2 ($X = \text{S}, \text{Se}, \text{Cl}, \text{Br}$) Monolayers and Their Electronic Properties using Ab-initio approach.

P09 - DUTT Rajeev

Electronic, mechanical, vibrational and thermoelectric properties of Chalcogens

P10 - EL-ACHARI Tarik

Study of Magnetic, Electronic and Thermodynamic Properties in Transition Metals-doped zinc-blende MgS and MgSe : Ab-initio calculations.

P11 - GILANI Shazma

3d-Electron-Doping Induced Multiferroicity and Half-Metallicity in PbTiO_3

P12 - GUPTA Naveen

Stimulated Raman Scattering of Elliptical q-Gaussian Laser Beams in Narrow Bandgap Semiconductors with Ramp Shaped Doping Profile

P13 - KAUR Jagjit

Tuning Spin Texture and Spectroscopic Limited Maximum Efficiency through Chemical Composition Space in Double Halide Perovskites

P14 - KOLOS Miroslav

Giant Linear and Nonlinear Excitonic Responses in an Atomically Thin Indirect Semiconductor Nitrogen Phosphide

P15 - KUMAR Nikhil

FIRST-PRINCIPLES INVESTIGATIONS OF VARIOUS PHYSICAL PROPERTIES OF NdN UNDER HIGH PRESSURE AND HIGH TEMPERATURE

P16 - KUMAR Vipin

Electric field-induced band modulation of predicted ternary 2D MXC₃ [M:X = As:Ge, Sb:Sn and Bi:Pb] with strong stability and optical properties

P17 - LEJIBO Tigistu Tesfahun

Classification of rose flowers based on Fourier descriptors and color moments

P18 - LIN Changpeng

General invariance and equilibrium conditions for lattice dynamics in 1D, 2D, and 3D materials

P19 - LIU Jing

Electric-field-driven excitonic instability in an organometallic manganese-cyclopentadienyl wire

P20 - MANAI Soumaya

Ab-initio Many-Body perturbation theory of doubly excited states of Helium-Like Iron.

P21 - MARINHO JUNIOR Enesio

Optoelectronic properties of transition dichalcogenides for photovoltaic applications: GW and Bethe-Salpeter study

P22 - MULATU Tadesse Abebe

optical property of hydrogen molecule absorption on silicon carbide nanotube

P23 - MUSARI Adebayo Abolore

Lattice dynamics, Elastic, Magnetic, Thermodynamic and Thermoelectric Properties of Two-dimensional MPSe₃ (M = Cd, Fe and Ni) Materials

P24 - ODEYEMI Olusanmi Ebenezer

First Principle Calculations of Structural, Electronic, Magnetic, Mechanical and Thermodynamic Properties of XCrGe (X = Hf and Zr) Half-Heusler compounds

P25 - OLOPADE Abayomi Muteeu

THE ELECTRONIC, STRUCTURAL AND OPTICAL PROPERTIES OF BARIUM PEROVSKITE COMPOUND

P26 - OSAFI Eromwon Omosede

Optical properties of Zn doped AgInSe₂ Chalcopyrite semiconductor.

P27 - OYENIYI Ezekiel

Study of the electronic and optical properties of antiperovskite Mg₃XN (X=P, As, Sb, Bi): The GW/BSE approach

P28 - PAEZ ORNELAS José Israel

Understanding the role of oxygen Vacancies in the stability of ZnO(0001)-(1 × 3) surface reconstructions: a DFT study

P29 - RAVAL Dhara Vasantkumar

Adsorption of noxious H₂S and HF Gases on 2D Penta-PdAs₂ Semiconductor as Gas Sensor : A DFT Study

P30 - ROMANIN Davide

Topological excitonic transition in organic polymers: singlet fission and negatively dispersing excitons

P31 - SAEED Yasir

Cs₂NaGaBr₆ : A New Lead-Free Halide Double Perovskite with DirectBand Gap

P32 - SYED Abbas Zuhair

Lead free double-perovskites based on thallium for thermoelectric and photovoltaic applications: A first-principle study of structural, optoelectronic and thermoelectric properties

P33 - THACKER Prakashchandra Bhavik

Structural Vibrational, thermophysical and Electronic properties of L10 FePt and FePd

P34 - YADAV Kumar Pushendra

Excitons in MoSi₂Z₄ Family of 2D materials

Electronic and Thermoelectric Properties of Half-Heusler Semiconductors XHfSn (X = Ni and Pt)

Abstract In this work, detailed density functional theory calculations were performed to obtain the electronic and thermoelectric properties of ternary semiconductors XHfSn (X = Ni and Pt) with half-Heusler structures. We report the band gaps of 0.38 and 0.97 eV for NiHfSn, and PtHfSn respectively, indicating the narrow gaps of these compounds. The partial density of state for these two compounds reveal that the top of their valence bands is marjorly composed of Sn 2p states and Hf 4d states. The conduction band minimum (CBM) of NiHfSn, on the other hand, is mainly constituted of Hf 4d states and a small part from N 3d states while for PtHfSn, we have contributions majorly from Hf 4d states and a tiny part from Pt 4d states. The calculated Seebeck coe_cients for NiHfSn and PtHfSn, are 63.36 and 66.30 $\mu\text{V}/\text{K}$ respectively at 300 K which increased to peak values of 151.68 and 159.62 $\mu\text{V}/\text{K}$ respectively at 1200 K. The power factor per relaxation of NiHfSn and PtHfSn increases with temperature. Of these two materials, our results screened PtHfSn to be better for thermoelectric application.

Absorption spectra for small pigment molecules: Comparing real-time TDDFT with Linear-response approach

The performance of real-time TDDFT has been assessed, and its capability to examine optical response at high energies has attracted increasing attention in recent years. In the current work, the optical response of a category of tiny pigments has been explored employing real-time, and linear response approaches. While obtained results from the two approaches are in reasonable agreement for higher energies, optical spectra at the lower energies are more demanding than real-time methods. In this regard, carefully adjusting the simulation time, time steps, and post-process is investigated. A promising approach is suggested for calculating real-time-based spectra using the LR-TDDFT results at lower energies.

Prediction of Large Intrinsic Ferroelectricity in Monolayer Silicon Carbide

As a direct wide bandgap semiconducting ferroelectric material, two-dimensional, 2D, silicon carbide has the potential to bring revolutionary advances into optoelectronic and electronic devices. It can overcome current limitations with silicon, bulk SiC, and gapless graphene. In addition to SiC, which is the most stable form of monolayer silicon carbide, other compositions, i.e., XC , are also predicted to be energetically favorable. Depending on the stoichiometry and bonding, monolayer SiC may behave as a semiconductor, semimetal or topological insulator. With different Si/C ratios, the emerging 2D silicon carbide materials could attain novel electronic, optical, magnetic, mechanical, and ferroelectric properties that go beyond those of graphene, silicene, and already discovered 2D semiconducting materials. This paper summarizes key findings in 2D SiC and provides insight into how changing the arrangement of silicon and carbon atoms in SiC will unlock incredible optoelectronic, ferroelectric properties.

Intermediate band governed enhancement of photo-responsive nature for Fe-loaded and O-doped g-C₃N₄

B.R. Bhagat and Alpa Dashora*

Computational Material Science Laboratory, Department of Physics,

The M. S. University of Baroda, Vadodara 390002, India

** Email: brajesh.b-phyphd@msubaroda.ac.in*

Enhancing the surface capability of graphitic carbon nitride (g-C₃N₄) for high optical absorbance and reaction-intermediate adsorption requires activation of p_z orbital, achieved by inducing impurity state through doping/decoration of non-metal (NM)/transition metal (TM) atom. $p_\pi-d_\pi$ interaction between N-TM atom and NM-TM atom governs the charge separation and built-in electric field [1, 2]. Present work on pristine, O doped-, Fe loaded- and Fe-O-g-C₃N₄ (loaded-doped) performed using Wien2k code [3, 4] utilizing full-potential linearized augmented plane wave method display increased electron localization and reduced planar sp^2 hybridization compared to pristine g-C₃N₄. High electron mobility and heavy holes in O-g-C₃N₄ and Fe-O-g-C₃N₄ lead to reduced recombination rate. As compared to pristine, 5 fold increment in integrated absorption coefficient, 3.8 times decrement in work function for efficient charge transfer occurring at intermediate-substrate interface and formation of a wide intermediate state in Fe-O-g-C₃N₄ directs towards its effective photo-reactivity. Hybridization of $Fe-3d$ with $O-2p$ in the forbidden region, their dipole interaction, charge cloud formation over edge N and $p_\pi-d_\pi$ interaction between N-Fe & O-Fe provides deep trap site increasing charge carrier recovery time, activating surface for intermediate adsorption providing potential applications of Fe-O-gC₃N₄ as efficient photocatalyst.

[1] B.R. Bhagat et al., Carbon, **178**, 666 (2021).

[2] Y. Zhang et al., Ceramics International, **48(3)**, 4031 (2022).

[3] P. Blaha et al., J. Chem. Phys., **152**, 074101 (2020).

[4] F. Tran et al., Phys. Rev. Lett., **102**, 226401 (2009).

Tailoring thermal properties of High Entropy Oxides: new technologies for radiative passive cooling against global warming

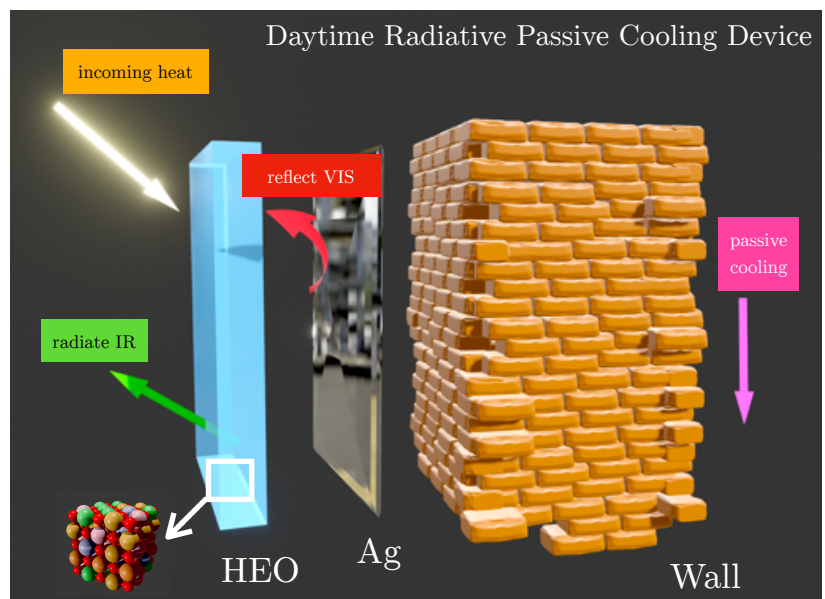
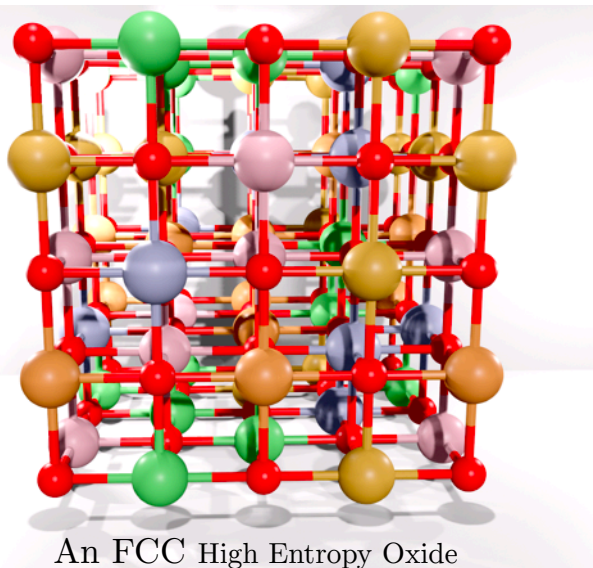
Costanza Borghesi¹, Giacomo Giorgi¹

¹Department of Civil & Environmental Engineering (DICA), Università degli Studi di Perugia, Via G. Duranti 93, 06125 Perugia, Italy

Approximately 10% of global CO₂ emissions are generated by cooling devices such as air conditioners, and, with the growing demand for air conditioning systems, electricity consumption is increasing exponentially. Electricity is still produced mainly from non-renewable fossil fuels and most air conditioning systems use chlorofluorocarbons as refrigerants: these greenhouse gases are thousands of times more harmful than CO₂. As long as we depend on fossil fuels and traditional cooling devices, we will fight the problem of global warming while continuing to pollute air. Just recently, passive radiative cooling systems have received attention as they can decrease the temperature through the intrinsic properties of the materials and devices used in these systems without consuming energy from other sources.

The novelty of radiative cooling lies in its ability to achieve cooling without any extra input energy. This passive cooling mechanism has the potential to dissipate excess heat from the earth to the universe, especially in the coming decades, with the increasing likelihood of extreme heatwaves as a result of climate change. With this emergence of advanced design and fabrication cooling technologies, new classes of selective infrared radiators, including photonic structures and meta-materials, have been rapidly developed in recent studies¹.

Among them, High Entropy Oxides (HEO) are new categories of ceramics that have very promising, but yet to be explored, properties where five or more elemental components are incorporated into a single lattice arbitrarily as it has been suggested that the entropic influence to the free energy is what drives the thermodynamic stability, instead of the cohesive energy². The multicomponent design could expand the available compositional space contributing to meeting the demands on today's advanced materials and for such reason the present research scope is to investigate the structural and thermal properties of the mentioned class of materials, in order to achieve stable and efficient radiative layers for passive cooling devices. Indeed, while HEOs offer a significant opportunity for functional material applications, their inherent clutter and highly localised chemical environments bring with them new challenges. Thus, a deeper investigation should be carried out, with the support of theoretical and experimental work, to understand the effects that the disorder has on the structure to discover and ultimately exploit the extraordinary possibilities of HEOs.



References:

¹Bin Zhao, Mingke Hu, Xianze Ao, Nuo Chen, Gang Pei, Radiative cooling: A review of fundamentals, materials, applications, and prospects, *Applied Energy*, Volume 236, 2019, Pages 489-513, ISSN 0306-2619, <https://doi.org/10.1016/j.apenergy.2018.12.018>.

²Shaima H. Albedwawi, Asala AlJaberi, Gregory N. Haidemenopoulos, Kyriaki Polychronopoulou, High entropy oxides-exploring a paradigm of promising catalysts: A review, *Materials & Design*, Volume 202, 2021, 109534, ISSN 0264-1275, <https://doi.org/10.1016/j.matdes.2021.109534>.

Deterministic control of ferroelectric polarization by ultrafast laser pulses

Ultrafast light-matter interactions present a promising route to control ferroelectric polarization at room temperature, which is an exciting idea for designing novel ferroelectric-based devices. One emergent light-induced technique for controlling polarization consists in anharmonically driving a high-frequency phonon mode through its coupling to the polarization. A step towards such control has been recently accomplished, but the polarization has been reported to be only partially reversed and for a short lapse of time. Such transient partial reversal is not currently understood, and it is presently unclear if a full control of polarization, by, e.g., fully reversing it or even making it adopt different directions (thus inducing structural phase transitions), can be achieved by activating the high-frequency phonon mode via terahertz pulse stimuli. Here, by means of realistic simulations of a prototypical ferroelectric, we reveal and explain (1) why a transient partial reversal has been observed, and (2) how to deterministically control the ferroelectric polarization thanks to these stimuli. Such results can provide guidance for realizing original ultrafast optoferroic devices.

Koopmans spectral functionals in periodic-boundary conditions

Koopmans spectral functionals aim to describe simultaneously ground state properties and charged excitations of atoms, molecules, nanostructures and periodic crystals. This is achieved by augmenting standard density functionals with simple but physically motivated orbital-density-dependent corrections. These corrections act on a set of localized orbitals that, in periodic systems, resemble maximally localized Wannier functions. At variance with the original, direct supercell implementation [Phys. Rev. X **8**, 021051 (2018)], we discuss here i) the complex but efficient formalism required for a periodic-boundary code using explicit Brillouin zone sampling, and ii) the calculation of the screened Koopmans corrections with density-functional perturbation theory. The implementation in the Quantum ESPRESSO distribution and the application to prototypical insulating and semiconducting systems are presented and discussed.

Thermal Stability of NbX₂ (X= S, Se, Cl, Br) Monolayers and Their Electronic Properties using *Ab-initio* approach.

Anjna Devi^{1,2, a)} Arun Kumar^{2, b)}, Amarjeet Singh^{1, c)}

¹Department. of Physics, Himachal Pradesh University, Shimla, H. P., 171005 (India)

²Department. of Physics, Swami Vivekanand Government College Ghumarwin, Bilaspur, H. P., 174021 (India)

^{a)}anjnahpu90@gmail.com

^{b)}arun242493@yahoo.com

^{c)}amarjeet.sirohi@gmail.com

Keywords: DFT, Monolayer, Transition metal dichalcogenes, Transition metal dihalogens.

EXTENDED ABSTRACT: We report Density Functional Theory (DFT) based electronic properties of NbX₂ (X= S, Se, Cl, Br) monolayers. Thermal stability also reported by calculating phonon spectrum and we observed that all the systems are thermally stable. Each optimized structure have different binding energies in which transition metal dichalcogenes NbX₂ (X=S, Se) have large value and hence more stable as compared to transition metal dihalogens NbX₂ (X=Cl, Br). Also NbX₂ (X=S, Se) have magnetic moment which is due to spin contribution of Nb atoms. All the systems are metallic in nature with conductance of 4G₀. These properties help us in fabrication of electronic devices.

Systems	Lattice Constant	Average bond length (Nb-X ₂) (Å)	Binding energy (E _b) (eV)	Band gap (E _g) (eV)	Magnetic moment	Conductance (G ₀)
NbS ₂	3.364 (3.35) ¹	2.504	5.358	0	0.4706	4
NbSe ₂	3.357 (3.48) ¹	2.650	4.861	0	0.6158	4
NbCl ₂	3.247	2.595	4.194	0	0	4
NbBr ₂	3.245	2.726	3.719	0	0	4

REFERENCES

- 1) Zhou, Yungang, Wang, Zhiguo Yang, Ping Zu, Xiaotao Yang, Li Sun, Xin Gao, Fei, "Tensile Strain Switched Ferromagnetism in Layered NbS₂ and NbSe₂", *ACS nano*, vol.6, 1936-0851, 2012.
- 2) Anjna Devi, Arun Kumar, P.K. Ahluwalia, Amarjeet Singh, "Novel properties of transition metal dichalcogenides monolayers and nanoribbons (MX₂, where M = Cr, Mo, W and X = S, Se): A spin resolved study" *Materials Science and Engineering B* 271 (2021) 115237.
- 3) Suruchi Thakur, Narender Kumar, Raj Kumar, Anjna Devi, and Arun Kumar, "Band gap engineering of tungsten disulfide (WS₂) nanoribbon by applying elastic strain and electric field" 2265, 030698 (2020).

Electronic, mechanical, vibrational and thermoelectric properties of Chalcogens

In the present work, we explore half Heusler alloys (HHAs) based on various chalcogen atoms, with 18 valence electrons (VEC) per unit cell, namely, $A(=Sc, Y, La)B(=Co, Rh)C(=S, Se, Te)$. Systematic density functional theory (DFT) based investigations have been carried out to probe their energetic, mechanical and lattice dynamical properties. Following that, analyses of band structure and constant energy surface reveal high values of valley degeneracy in the states near the Fermi energy in many of these alloys. Further, the dependence of the thermoelectric properties (TEP) on the carrier concentration, chemical potential and temperature for the n- and p-type doped systems have also been studied. In comparison to the well-known TiNiSn alloy, for most of the probed HHAs, about 10% enhancement has been found in the maximum values of figure of merit calculated using only the electronic contribution of thermal conductivity (ZT_e)_{max}.

Study of Magnetic, Electronic and Thermodynamic Properties in Transition Metals-doped zinc-blende MgS and MgSe: Ab-initio calculations.

Electronic thermodynamic and magnetic properties of the zinc-blende Magnesium Sulfide (MgS) and Magnesium Selenide (MgSe) doped with several transition metals (Ti, V, Cr, Mn, Co, and Ni) are studied using the density functional theory (DFT), namely the KKR-CPA-PBE method. Pure MgS and MgSe is a wide bandgap semiconductor, and doping it with transition metals single impurities generate ferromagnetic half-metallic behavior. The values of the formation energy reveal that our systems are stable systems for all impurities concentrations. The ferromagnetic state is found to be the stable phase for all compounds except the Mn doping case. The total magnetic moments increase linearly when increasing doping impurities, and finally, the Curie temperature is calculated using the mean-field approximation, showing significant values. The present findings reveal transition metals-doped zincblende transition metals-doped zincblende MgS and MgSe as potential candidates for high Curie temperature ferromagnetic materials and Spintronics devices.

3d-Electron-Doping Induced Multiferroicity and Half-Metallicity in PbTiO₃

Atomic interactions can be used to control and tune the physical properties of the systems, which are different from the pristine structure. Herein, we explored the ferroelectric, magnetic, and electronic properties of 3d transition metals (TM = Sc, V, Cr, Mn, Fe, Co, Ni, Cu, and Zn)-doped PbTiO₃ utilizing density functional theory calculations. The stability of doped systems is analyzed by computing formation energies, which exhibit a strong interdependence on the dopant atomic numbers. It is established that the versatile multiferroic properties can be obtained by TM-doping, which are ranging from non-magnetic (Sc-, Zn-, and Ni-doped systems)/magnetic (V-, Mn-, Fe-, and Cu-doped systems) semiconductor or conductor to half-metallic ferromagnetic (Cr and Co-doped systems). The most striking feature of the present study is that Cr- and Co-doped systems display half-metallic behavior along with a moderate value of spontaneous polarization. The metallicity in the spin-minority channel mainly comes from the Cr and Co 3d_{yz+zx} orbitals with a small contribution from d_{xy}. Finally, the induced magnetism in these doped systems is explained by addressing the low and high spin state configurations of TM ions. Hence, our calculations highly demand the experimental verification of these doped materials for their potential realization in spintronic devices.

Stimulated Raman Scattering of Elliptical q-Gaussian Laser Beams in Narrow Bandgap Semiconductors with Ramp Shaped Doping Profile

Stimulated Raman scattering (SRS) of elliptical q-Gaussian laser beams interacting with narrow bandgap semiconductors with axially inhomogeneous doping profile has been investigated theoretically. An intense laser beam propagating through narrow bandgap semiconductor gets coupled with a pre existing electron plasma wave (EPW), due to relativistic mass nonlinearity of conduction electrons. This nonlinear interaction of pump beam with EPW produces a back scattered wave whose frequency is the difference between the frequencies of pump wave and EPW. Using variational theory semi analytical solutions of the coupled nonlinear wave equations for the three waves (pump, EPW and scattered) have been obtained under W.K.B approximation technique. It has been observed that self focusing of the laser beam significantly affects the power of back scattered wave.

Tuning Spin Texture and Spectroscopic Limited Maximum Efficiency through Chemical Composition Space in Double Halide Perovskites

Jagjit Kaur and Sudip Chakraborty*

*Materials Theory for Energy Scavenging (MATES) Lab, Harish-Chandra Research Institute
(HRI) Allahabad, Chhatnag Road, Jhunsi, 211019, India.*

E-mail: sudipchakraborty@hri.res.in, sudiphys@gmail.com

Abstract

The Double halide perovskite family is emerging as a promising alternative to lead-based hybrid perovskite materials not only in energy scavenging but also in spin-optoelectronic applications. In this study, we have envisaged the electronic and optical properties along with spin-texture for $\text{Cs}_2\text{AgBiBr}_6$ using density functional theory (DFT). As this is the first time to the best of our knowledge, the aforementioned properties are explored for antimony substituted $\text{Cs}_2\text{AgBiBr}_6$. Interestingly, we have observed Rashba like spin switching from the in-plane spin texture in the $k_x - k_y$ plane centered at the Γ point despite the centrosymmetric crystal structure of $\text{Cs}_2\text{AgBiBr}_6$, which is remarkable for the double halide perovskite family. This particular finding could pave the way towards spinorbitronics applications, while one can coin this phenomenon as a pseudo-Rashba effect due to the absence of broken inversion symmetry. We have thoroughly investigated the spectroscopic limit maximum efficiency (SLME) for solar energy applications.

Giant Linear and Nonlinear Excitonic Responses in an Atomically Thin Indirect Semiconductor Nitrogen Phosphide

Large linear and nonlinear optical responses can be obtained from two-dimensional semiconductors with an indirect electronic gap. Here, we demonstrate exceptionally large exciton-driven responses such as the fundamental exciton binding energy (2 eV), zero-point band-gap renormalization (200 meV), and nonlinear second and third harmonic coefficients (800 pm/V and 1.4×10^{-18} m²/V², respectively) from an atomically thin binary group-V nitrogen phosphide (NP) semiconductor. The influence of lattice vibrations on the absorption spectra unfolds strong electronic couplings to both LA and ZO-TO phonon modes. All the linear process analyses were computed using a fully ab initio-based G₀W₀ + Bethe–Salpeter equation approach that also includes the electron–phonon self-energies. The nonlinear processes were instead obtained using a real-time ab initio process flow after creating a coupling between the time-dependent external electric field and the correlated electrons within the modern theory of polarization and the same electron–hole interaction level.

FIRST-PRINCIPLES INVESTIGATIONS OF VARIOUS PHYSICAL PROPERTIES OF NdN UNDER HIGH PRESSURE AND HIGH TEMPERATURE

Nikhil Kumar* and Sanjay Kumar Singh

Goswami Ganesh Dutt Innovation Hub, Department of Physics, S. D. College, Barnala-148101, Affiliated to Punjabi University, Patiala, Punjab, India

*E-mail: niks987100ni@gmail.com

Abstract: We have computed the various physical properties i.e., structural, phase transition, magnetic and thermal properties of Neodymium Nitride compound (NdN). The calculations have been performed within Density functional theory (DFT), using the full potential method and a quasi-harmonic Debye model as implemented in the WIEN2k and GIBBS code respectively. Structural properties viz, lattice constant (a), bulk modulus (B_0) and its pressure derivative (B_0') and total energy (E_0) have been calculated in NaCl and CsCl i.e., B1 and B2 phase respectively. Our calculated lattice constant is 5.105 Å which agrees well with experimentally measured value 5.132 Å. The high pressure phase transition has been observed from B1-Phase to B2-phase at 52.96 GPa. Apart from this we have also computed the thermal parameters such as Gruneisen parameter, Debye temperature, specific heat and thermal expansion coefficient as a function of pressure and temperature. The computed value of Debye temperature is 413.39 K at ambient condition which agrees well with the experimental value 410 K with 0.82% inaccuracy.

Keywords: Density Functional Theory, WIEN2k, GIBBS Code, Thermal Properties and Neodymium Nitride.

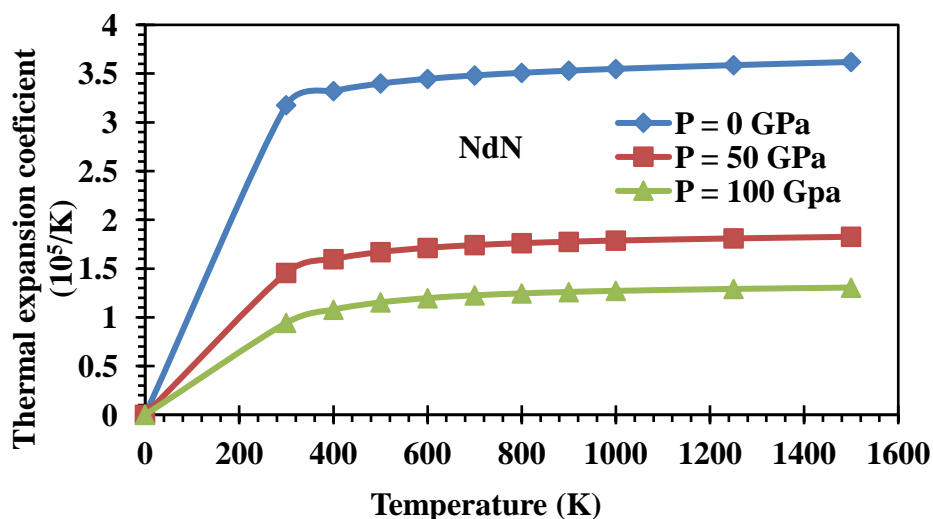


Figure 1. Variation of thermal expansion coefficient ($10^5/K$) with temperature (K).

Electric field-induced band modulation of predicted ternary 2D MXC₃ [M:X = As:Ge, Sb:Sn and Bi:Pb] with strong stability and optical properties

The present work reports a new series of ternary two-dimensional MXC₃ [M:X = As: Ge, Sb: Sn and Bi: Pb] compounds whose stability and existence are confirmed through the phonon dispersion analysis, elastic properties and ab initio molecular dynamics simulation. The developed compounds are further investigated with their electronic and optical properties using density functional theory. We have observed zero bandgap nature in MXC₃ compounds, where AsGeC₃ shows the graphene-like band structure with Dirac cone at K-point. We have systematically applied the external electric field up to ± 0.40 eV/Å to modulate the electronic and optical properties of these compounds. The increasing magnitude of the electric field has shown the increasing nature of bandgap in the AsGeC₃ compound, while no effect was observed in case of SbSnC₃ and BiPbC₃ compounds. Consequently, the bandgap of AsGeC₃ compound is tuned up to 0.98 eV which is maximum at an optimum value of the applied electric field of ± 0.40 eV/Å. All the three 2D MXC₃ compounds have shown the broken symmetry of the structure after the optimum value of the electrical field that can be understood by the maximum tolerance limit of an applied electric field. Our results strongly suggest the excellent mechanical stability of the AsGeC₃ compound under the applied electric field. We have also calculated the variation in the optical properties upon the external field for the AsGeC₃ compound, which shows a good transparency nature and can be used in the regulation of the smart window applications.

Classification of rose flowers based on Fourier descriptors and color moments

In this paper, a rose-flower variety classification scheme, using color and shape features is presented. The first three statistical moments of the R, G, and B planes of the image were calculated to describe the color, while Fourier coefficients are used to describe the shape. For shape description, signatures (wave-forms) of the boundary contour of the binary images were extracted. Fourier coefficients that are used to describe the shape were estimated using the signatures generated. Depending on the Fourier coefficients, a representation of sums of angles formed along the boundaries of the flowers was defined. Using these sums and the color features as input to an artificial neural network (ANN), the flowers were classified into their respective target classes. The eighteen flower varieties considered in this study were classified with an accuracy of 95.6%, 98.9%, and 100% using their shape, color, and combination of both shape and color features, respectively. Comparing these results, it was found that the combination of the two features is an efficient criterion for rose flower variety discrimination and classification.

P18 General invariance and equilibrium conditions for lattice dynamics in 1D, 2D, and 3D materials

Changpeng Lin,^{1,2} Samuel Poncé,^{3,1} and Nicola Marzari^{1,2}

¹*Theory and Simulation of Materials (THEOS), École Polytechnique Fédérale de Lausanne, CH-1015 Lausanne, Switzerland*

²*National Centre for Computational Design and Discovery of Novel Materials (MARVEL),*

École Polytechnique Fédérale de Lausanne, CH-1015 Lausanne, Switzerland

³*UCLouvain, Institute of Condensed Matter and Nanosciences (IMCN),*

Chemin des Étoiles 8, B-1348 Louvain-la-Neuve, Belgium

The existence of a quadratic or linear flexural acoustic (ZA) branch in low-dimensional (LD) system in the long-wavelength limit is still actively debated. The related lattice-dynamical properties play a vital role in carrier transport, phonon-assisted optics, superconductivity, and thermoelectrics. Here, we present invariance and equilibrium conditions of the lattice potential that allows to recover the quadratic dispersion of flexural phonons in LD materials around the Brillouin zone center, in line with the phenomenological models for long-wavelength bending modes. In the context of long-wavelength acoustic waves, we prove that for any LD material the bending mode can have a pure polarization in the vacuum direction and a quadratic dispersion in the long-wavelength limit. In addition, we propose an effective polar scheme for treating the invariance conditions in crystals with non-vanishing Born effective charges. The long-range dipole-dipole interaction induces a contribution to the stress tensor which must vanish to recover the quadratic dispersion of ZA phonons in LD system. Our approach has been successfully applied to the phonon dispersion of over 160 2D materials. Our findings open new avenues for the lattice-dynamical studies of novel LD materials.

Electric-field-driven excitonic instability in an organometallic manganese-cyclopentadienyl wire

Jing Liu Yuanchang Li*

School of Physics, Beijing Institute of Technology, Beijing 100081, China



Abstract

Excitonic insulator is a macroscopic quantum system whose ground state consists of spontaneously formed and condensed excitons. While various excitonic insulators have been explored, they are almost exclusively characterized by the condensation of dark (optically inactive) excitons. Our first-principles GW -BSE calculations show that a transverse electric field will drive an organometallic manganese-cyclopentadienyl wire into a unique “bright” excitonic insulator phase, as the combined consequence of giant Stark effect and electric-field-induced symmetry breaking. Such bright excitonic insulators can be directly identified by experiment due to their coherent radiation. Our results are not only of scientific interest in electric-field control of exciton condensation, but may also open an opportunity to create a coherent light source based on the excitonic insulator.

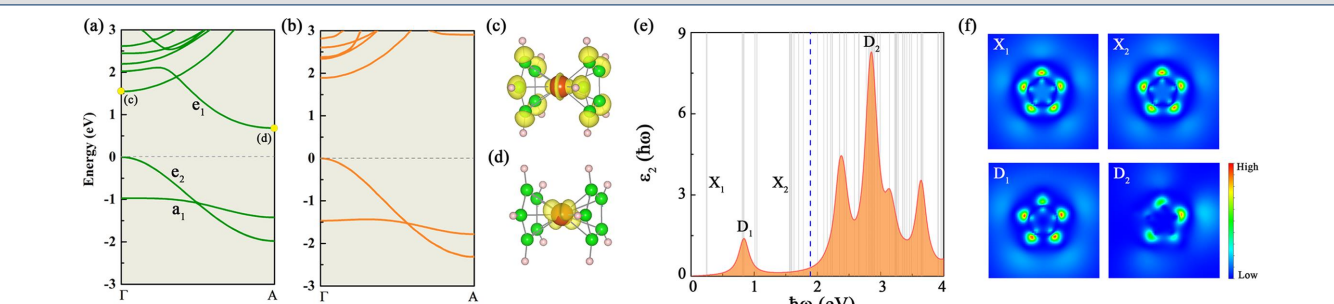
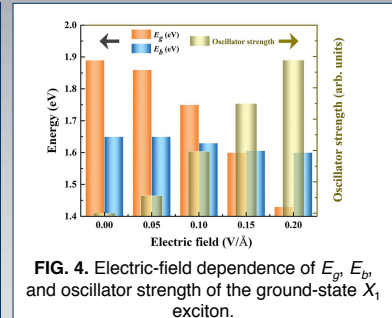
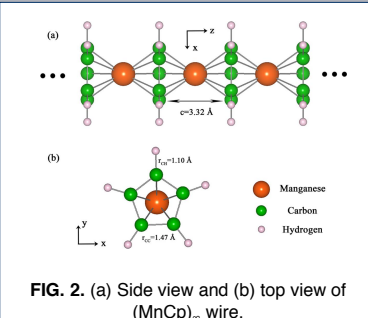
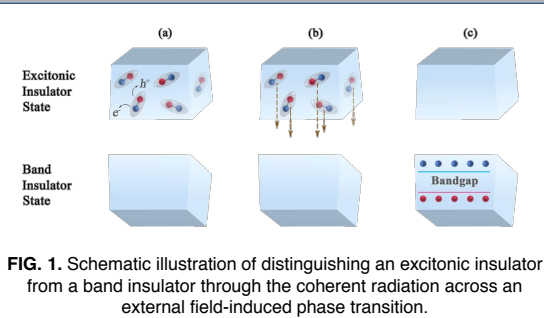


FIG. 3. Band structures respectively calculated by (a) PBE and (b) G_0W_0 methods. (c), (d) Decomposed charge densities corresponding to the states marked in (a) (yellow dots). (e) Exciton energies (gray vertical lines) superimposed on the imaginary part of the BSE dielectric function. (f) Two-dimensional cross section of the real space exciton wave functions for the states noted in (e).

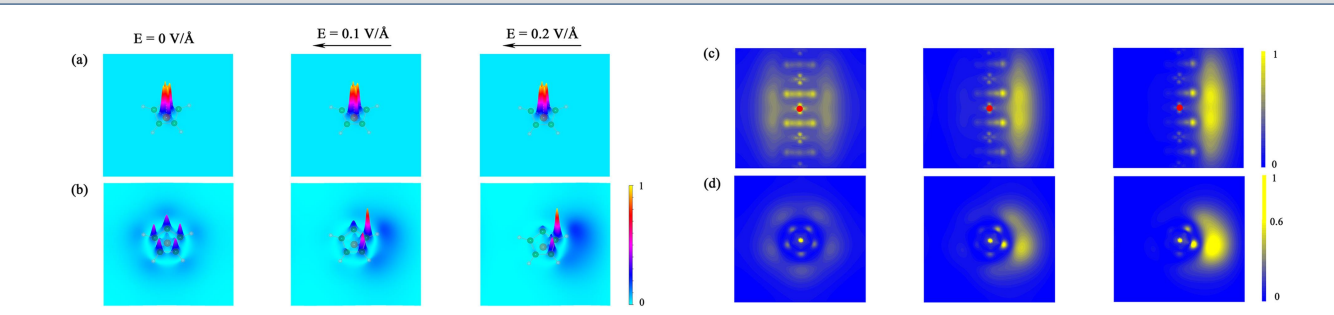


FIG. 5. Decomposed charge densities at the point for the (a) top valence band, and (b) bottom conduction band under zero, $E = 0.1$ V/Å and $E = 0.2$ V/Å electric field. (c) Side view and (d) top view of the real-space exciton wave functions for the X_1 under zero, $E = 0.1$ V/Å, and $E = 0.2$ V/Å electric field.

Conclusion

In conclusion, first-principles calculations using the prototype $(\text{MnCp})_\infty$ show a new kind of bright excitonic insulators that have not yet been recognized by the research community. Its unique fingerprint is embodied in the electron-hole coherent radiation recombination across an excitonic-insulator–band-insulator phase transition, which therefore allows the experimental identification with certainty. By contrast, such coherent radiation does not exist in the dark excitonic insulator. A practical concern is which materials are suitable for tuning into the bright excitonic insulator via the mechanism proposed here. Of course, not any band insulator can serve this purpose, even if a giant Stark shift is achieved. Instead, ones need to focus on materials that break the synergy between E_g and E_b so that applying an external field can reverse the relative size of the two. Generally, such materials are characterized by the forbidden transitions between the bandedge states. Our work thus provides a prospect for exciton manipulation in low-dimensional systems, as well as construction of coherent optical devices based on the excitonic insulators.

PHYSICAL REVIEW B 104, 085150 (2021)

FOR MORE INFORMATION:

* Corresponding author. E-mail address: yuancli@bit.edu.cn

Jing Liu. Phone: 18515397566



Ab-initio Many-Body perturbation theory of doubly excited states of Helium-Like Iron

Soumaya Manai^{1,2}, Dhia Elhak Salhi¹ and Haikel Jelassi¹

¹*Research laboratory on Energy and Matter for Nuclear Science Development, LR16CNSTN02, Tunisia.*

National Center for Nuclear Science and Technologies, Sidi Thabet Technopark 2020 Ariana Tunisia.

²*Faculty of Sciences of Bizerte, University of Carthage, Tunisia.*

The Many-Body Perturbation theory (*MBPT*) has been included within the Flexible Atomic Code [1] and successfully used in calculating atomic parameters of high accuracy [2, 3, 4]. This method attempts to solve the Dirac equation and a perturbation potential by a model potential including the screening effects of all electrons, which is approximated by a local central potential derived from a Dirac-Fock-Slater self-consistent field calculation. It should be selected appropriately to minimize the potential for disturbance. The full integrity of the theoretical methods can be found in the Gu reference [1].

In this work, we used this approach to provide the energy levels and transitions rates arising from $2ln'l'(n' \leq 2, l' \leq (n' - 1))$ configurations of Helium-Like Iron. All theoretical energies are supplied with uncertainty estimates. Transition probabilities are reported for all *E1*, *E2*, *M1* and *M2* transitions. Breit interactions and quantum electrodynamics effects were included. Comparisons were made with other available theories reported in the literature [5, 6]. A good agreement between them has been found, which confirms the reliability of our results. The present complete and consistent results can be used to facilitate the identification of many observed spectral lines in astrophysical and plasma fusion.

- [1] M. F. Gu, Canadian Journal of Physics. **86** (2008) 675–689.
- [2] S. Manai and H. Jelassi, Pramana **95**, 1–9 (2021) (2021).
- [3] D. E. Salhi, S. B. Nasr, S. Manai and H. Jelassi, Results in Physics **23**, 103960 (2021).
- [4] S. Ben Nasr, S. Manai, D. E. Salhi, P. Quinet and H. Jelassi, Atomic Data and Nuclear Data Tables **135**, 101346 (2020).
- [5] G. W. Drake, Canadian Journal of Physics **66**, 586–611 (1988) .
- [6] Głowacki, Leszek, Atomic Data and Nuclear Data Tables **133**, 101344 (2020).

Optoelectronic properties of transition dichalcogenides for photovoltaic applications: GW and Bethe-Salpeter study

Transition metal dichalcogenides (TMDCs) are semiconductors with chemical configuration MX_2 , where M is a transition metal such as Mo, W, and X is a chalcogen atom as S, Se, or Te. TMDCs constitute a class of layered materials of significant interest for optoelectronics due to their scalability and thickness-dependent electrical and optical properties. Herein, we studied the electronic and optical properties of TMDCs composed of Mo, W, S, and Se within the G0W0 and Bethe-Salpeter approach. First-principles calculations based on density functional theory were carried out using the Quantum ESPRESSO package. The many-body perturbation theory and Bethe-Salpeter calculations were performed using YAMBO code. We further studied the photovoltaic performance of these TMDCs estimating the spectroscopic limited practical efficiency (SLME) in function of the thickness of the semiconductor. We compared the different TMDCs to known materials used in photovoltaics paving the way for efficient nanoscopically thin solar cells.

optical property of hydrogen molecule absorption on silicon carbide nanotube

Using the first-principles calculation, we investigate the adsorption and Optical Absorption Spectra of H₂ on (8, 0) silicon nanotubes (SiNTs). A detailed analysis of the structural and electronic properties of various optimized structures is performed. The results show that H₂ molecule can be chemisorbed on SiNT with the C atom bonding with the Si atom of the tubular surface when H₂ is located on the top,inner,center site, accompanying with the binding energy of 1.559 eV and charge transfer of 0.658e, which are larger than the results of other configurations. Most of the examined single-walled silicon carbide nanotubes (SWSiCNTs) exhibit the first strong absorption peak around 3 eV, while the (8, 0) SWSiCNT exhibits the first three strong peaks in the 1.5-4.0 eV region For the SiNT-NO systems, there exist four strong chemical adsorption configurations. The longitudinal screened polarizabilities of SWSiCNTs , suggesting the possibility of their aligned synthesis in electric fields .

Lattice dynamics, Elastic, Magnetic, Thermodynamic and Thermoelectric Properties of Two-dimensional MPSe₃ (M = Cd, Fe and Ni) Materials

A. A. Musari^{1,*} and Peter Kratzer^{2*}

February 17, 2022

¹ Physics with Electronics unit, Department of Science Laboratory
Technology, Moshood Abiola Polytechnic, PMB 2210, Abeokuta, Nigeria.
² Faculty for Physics, University of Duisburg-Essen, Lotharstraße 1, 47057
Duisburg, Germany.

Abstract

The recent scientific interest in 2D materials experienced exponential growth based on the huge potential in multifunctional applications such as optoelectronics, spintronics, nanocatalysis etc. Adopting Density Functional Theory (DFT) with Hubbard U correction implemented in Quantum Espresso, we have performed an extensive study of MPSe₃ monolayers (M = Cd, Fe and Ni). The computed electronic properties revealed the semi-conductive nature of the monolayers with small indirect bandgaps. A free-standing single layer of MPSe₃ can be exfoliated from the parent compound by virtue of their structural stability and high in-plane stiffness. Hence, the elastic and dynamical properties were computed to establish the mechanical and dynamical stability. The results showed that CdPSe₃ and NiPSe₃ are stable in hexagonal structure while the negative frequencies observed in the phonon dispersion of FePSe₃ indicate dynamical instability. The thermodynamic properties such as internal energies, vibrational free energies, entropies and constant-volume heat capacities have been computed within the harmonic approximations using the phonon density of states. The computed thermoelectric properties show that CdPSe₃ and FePSe₃ have the peak figure of merit at low temperature of 50 and 100 K respectively. This work also predicts poor thermoelectric performance for these investigated 2D materials at room temperature.

1 Introduction

Since the effective and remarkable exfoliation of graphene from graphite [1], the growing interest in the family of two-dimensional (2D) materials in the last

*authors to whom all correspondence can be made: musari.abolore@mapoly.edu.ng and peter.kratzer@uni-due.de

decades among experimental and theoretical scientists has been quite impressive. This can be fundamentally attributed to the fact that a large numbers of exfoliated two-dimensional compounds show strikingly different properties which make them more relevant for applications than their parent compounds in terms of multi-functional applications such as next-generation high-speed, low-power non-volatile memories, low dimensional spintronic, opto-electronics, sensors and actuators [2, 3, 4, 5, 6]. The family of 2D crystals besides graphene has considerably been dominated with new additions like boron nitrides [7, 8, 9, 10], layered compounds with a weak van der Waals (vdW) interaction between the layers such as transition metal dichalcogenides (TMDC) [11, 12, 13, 14, 15], transition metal trichalcogenides [16, 17, 18, 19, 20] and chromium trihalides [16, 21, 22, 23]. These compounds have been predicted to be highly suitable for wide range of electronic, thermal, optical mechanical and chemical applications [6, 16].

To illustrate the peculiar properties of 2D materials, we present some examples in more detail. For instance, single-layer MoS₂ for instance has been predicted to be direct band gap in the appropriate visible frequency range which has made it more suitable as next-generation opto-electronic and electronic devices when compared to its parent compound [3, 6]. Another peculiar property is magnetism in two dimensions, even in combination with semiconducting properties. The layered transitional metal tri-chalcogenides with structural formula ABX_3 where $A = \text{Mn}$ and Cr , $B = \text{Si}$ and Ge , while $X = \text{S}$, Se and Te have been studied widely as a promising candidate for 2D magnets [20, 24, 25]. In addition, metal phosphorus tri-chalcogenides MPX_3 , where M stands for divalent metal ions such as Mn , Cd , Fe , Ni , Cu , Zn etc. while $X = \text{S}$, Se and Te [17, 18, 26, 27, 28] have been predicted to be intriguing materials which can notably enhance the applications of 2D materials in a broad wavelength spectrum. Their exceptional and distinct structural, magnetic and physio-chemical properties have motivated this present study. In studying layered van der Waals materials, the ease of exfoliation of the single layer from the parent compound due their weak interlayer vdW interaction are measured by the cleavage energy. The cleavage energy is defined as the energy required to separate the crystal into two halves along the vdW gap between two successive layers. However, there is need to ensure there is no curling occurs during exfoliation, hence high stiffness is desirable. Therefore, the in-plane elastic constants were computed in this study. Also, the phonon dispersions for the monolayers were calculated to determine their dynamical stability.

We chose Cd , Fe and Ni for the divalent metal ions, with Cd being an example for an atom with a closed d -shell while Fe and Ni have partially filled $3d$ shells and thus may give rise to interesting magnetic properties. Experimentally, the cleavage energies of selenides, e.g. FePSe_3 , are in the range of 0.4 J/m^2 , see e.g. Ref. [29], and hence comparable to the cleavage energy of graphite. The crystal structures of MPSe_3 ($M = \text{Cd}$, Fe and Ni) monolayers are depicted in Figure 1. The subsequent section 2 presents the computational details while sections 3.1, 3.2, 3.3, 3.4, 3.5, 3.6 discuss the results. The summary of this work is given in section 4.

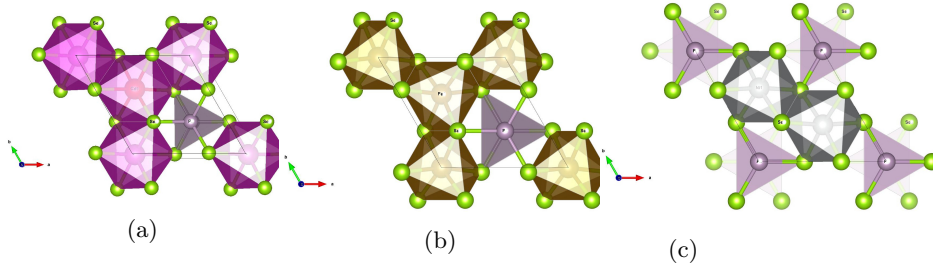


Figure 1: Crystal structure of (a) CdPSe₃ (b) FePSe₃ (c) NiPSe₃ monolayers

2 Computational Techniques

The present work was carried out using density functional theory (DFT) embodied in Quantum Espresso [30], using the projector-augmented-wave (PAW) method. The exchange-correlation functional as parameterised by Perdew, Burke and Ernzerhof was adopted [31]. These calculations also consider the van der Waals forces between the layers by adopting a correction based on DFT-D2 method of Grimme [32, 33]. The correction for strong on-site electronic correlation using an effective Hubbard parameter (GGA+U) is considered using the simplified version of Cococcioni and de Gironcoli [34] to treat the localized $3d$ electrons of Fe and Ni. Convergence test for the plane wave cutoff energy and k-point sampling were appropriately performed. For all the calculations a plane wave basis set expanded in energy with a cutoff of $75 Ry$. The k-point sampling with a mesh of $16 \times 16 \times 1$ Monkhorst-Pack [35] scheme were used for the single-layer systems. The converged plane-wave cutoff and k-point mesh were used to optimize the in-plane lattice constants and atomic coordinates until a maximum force on all atoms $< 10^{-5} Ry/a.u.$ was reached. A vacuum space of thickness 20 \AA is incorporated in order to avoid any interaction between images. The self-consistency convergence threshold of $10^{-10} Ry/a.u.$ was set for the total energies. The computed values of the equilibrium in-plane lattice constants and the magnetic ground state of semiconducting transition-metal trichalcogenide monolayers with their respective bond lengths, bond angles and cohesive energy of the compounds are presented in Table 1. The cohesive energy ΔE which is the measure of energetic stability of the structures of the single layers of MPSe₃ is calculated using

$$\Delta E = \frac{2\mu_M + 2\mu_P + 6\mu_{Se} - E_{MPSe_3}}{N} \quad (1)$$

where μ_M , μ_P and μ_{Se} are chemical potentials of M , P and Se atoms respectively, E_{MPSe_3} is the total energy of the MPSe₃ compounds per unit cell while N is the total number of atoms in a unit cell.

For the calculation of magnetic exchange interactions the four different magnetic configurations shown in Fig. 2 were employed. The exchange interaction parameters between spins were extracted by fitting the calculated total energies from various magnetic configurations to the Heisenberg spin Hamiltonian on a honeycomb lattice given by

$$H = J_1 \sum_{ij} \vec{S}_i \cdot \vec{S}_j + J_2 \sum_{ij} \vec{S}_i \cdot \vec{S}_j + J_3 \sum_{ij} \vec{S}_i \cdot \vec{S}_j \quad (2)$$

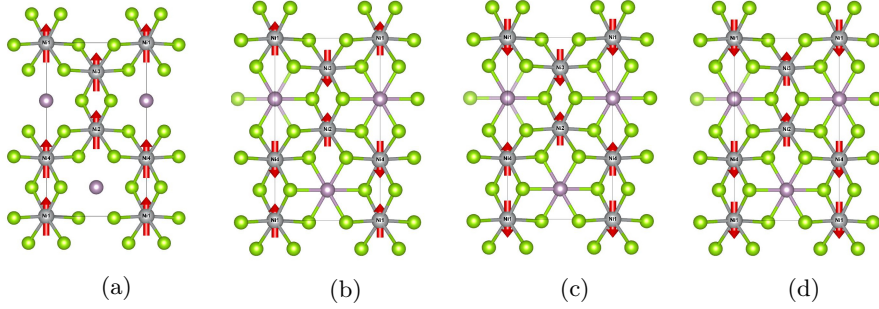


Figure 2: The possible magnetic configuration of NiPSe₃ monolayer (a) FM (b) AFM-Neel (c) AFM-zigzag configuration (d) AFM-stripy ordered

where $|S|$ is given as $1/2$ this corresponds to a magnetic moment of $1 \mu_B$ for Ni, $J_{1,2,3}$ are the exchange interactions between Nearest Neighbour (NN), second NN, and third NN spins. Using (2), the magnetic energy of two NiPSe₃ formulae can be expressed explicitly as equations (3) and (4):

$$E_{\text{FM/Neel}} = E_0 + (\pm 3J_1 + 6J_2 \pm 3J_3)|\vec{S}|^2 \quad (3)$$

$$E_{\text{AF-zigzag/stripy}} = E_0 + (\pm J_1 - 2J_2 \pm 3J_3)|\vec{S}|^2 \quad (4)$$

where E_0 is known as the ground state energy independent of the spin configuration.

The independent components of the elasticity tensor C_{11} , C_{12} and C_{66} are calculated by applying different, finite but small deformation (stretching or shearing) and computing the resulting energy.

The lattice dynamics of these 2D compounds are investigated by the computation of their phonon dispersion spectra. The phonon dispersion spectra were calculated along the high symmetry lines in the Brillouin zones using density functional perturbation theory (DFPT) [36, 37]. From the calculated phonon density of states, the thermodynamic properties of the lattice, such as the entropy and free energy at finite temperature, can be obtained.

The thermoelectric performance was characterized by computing the dimensionless figure of merit (zT), depending on temperature T and defined as

$$zT = \frac{S^2 \sigma T}{\kappa} \quad (5)$$

where S is the Seebeck coefficient defined in eq. 6 below, σ is the electrical conductivity given in eq. 7 while κ is the electronic part of the thermal conductivity expressed in eq. 8. The BoltzTraP code [38] was employed to solve semi-classical Boltzmann transport equation within the constant relaxation approximation to obtain energy, carrier concentration, temperature, Seebeck coefficient, electrical

Table 1: Calculated optimum in-plane lattice constants (\AA), Cohesive energies ΔE , bond length (\AA) and M-X-M bond angles for single layer MPSe_3

Comp.	Source	a	ΔE	M-M	M-Se	Se-Se	$\angle MXM$
CdPSe_3	This work	6.51	0.56	3.76	2.84	4.17	73.92°
FePSe_3	This work	6.11	0.53	3.53	2.42	3.60-3.69	76.14°
	Expt ^[39, 40]	—	—	3.62	2.66	- 3.60 -	84.5° ,
					2.69	3.64	87.9°
	Theory ^[28]	6.32	—	3.65,	2.65, 2.73	3.60, 3.64	84° ,
		6.13 ^[17]		3.71			87°
NiPSe_3	This work	6.14	0.52	3.54	2.53	3.42	92.16°

conductivity and thermal conductivity.

$$S_{\alpha\beta}(T, \mu) = \frac{1}{eT\Omega\sigma_{\alpha\beta}(T, \mu)} \int \bar{\sigma}_{\alpha\beta}(\varepsilon)(\varepsilon - \mu) \left[\frac{\partial f_o(T, \varepsilon, \mu)}{\partial \varepsilon} \right] d\varepsilon \quad (6)$$

$$\sigma_{\alpha\beta}(T, \mu) = \frac{1}{\Omega} \int \bar{\sigma}_{\alpha\beta}(\varepsilon) \left[- \frac{\partial f_o(T, \varepsilon, \mu)}{\partial \varepsilon} \right] d\varepsilon \quad (7)$$

$$\kappa_{\alpha\beta}^o(T, \mu) = \frac{1}{e^2T\Omega} \int \bar{\sigma}_{\alpha\beta}(\varepsilon)(\varepsilon - \mu)^2 \left[- \frac{\partial f_o(T, \varepsilon, \mu)}{\partial \varepsilon} \right] d\varepsilon \quad (8)$$

where Ω , e , f_0 and μ are the volume of the unit cell, the electronic charge, the Fermi-Dirac distribution in equilibrium at temperature T , and the chemical potential of the carriers, respectively.

3 Results and Discussion

3.1 Structural and Electronic properties

Firstly, the structures of MPSe_3 monolayers were optimized exclusively in non-magnetic, ferromagnetic and anti-ferromagnetic configurations. The energetically and magnetically most stable state for CdPSe_3 and FePSe_3 is obtained to be the non-magnetic configuration while NiPSe_3 is most stable in the Neel anti-ferromagnetic state. The optimised in-plane lattice constants, bond length bond angles and cohesive energy are presented in Table 1.

The nearest-neighbour M-M, M-Se and Se-Se distances as well as the bond angles in the optimized structure of MPSe_3 monolayers in their respective ground states are collected in Table 1. It is clearly seen that the computed values relatively agree with the available and accessible experimental results.

The knowledge of electronic properties of 2D MPSe_3 layers is essentially important to the understanding of their possible integration in nanodevices and also in spintronics applications for magnetic 2D materials. The band structures and their associated projected density of states for the most stable magnetic configuration of the three investigated materials are presented in Fig. 3. The band structures of the lowest spin configuration were computed using GGA+D2 approximation. All three MPSe_3 monolayers are predicted to be semiconductive in nature. The band gap for CdPSe_3 was obtained to be 1.24 eV, while the conduction band minimum (CBM) and valence band maximum (VBM) were

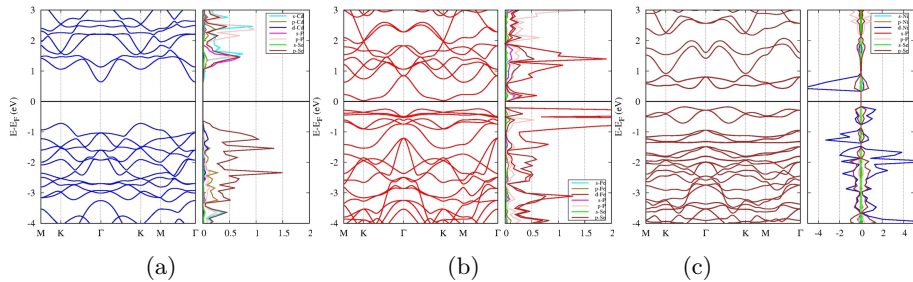


Figure 3: Band structures with respective projected density of states for (a) CdPSe₃ (b) FePSe₃ (c) NiPSe₃ monolayers

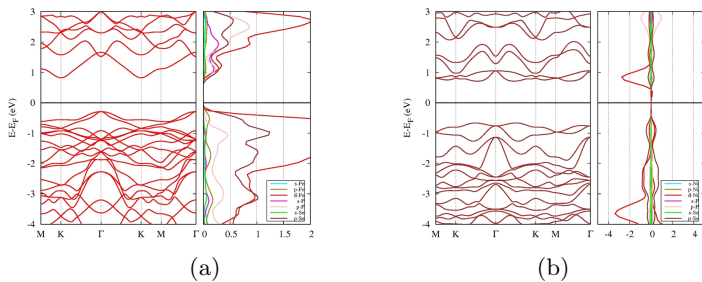


Figure 4: Band structures with respective projected density of states for with Hubbard $U = 4\text{eV}$ (a) FePSe₃ (b) NiPSe₃ monolayers

observed at the Γ and K points, respectively. While CdPSe₃ is found to be a wide-gap semiconductor, unrealistically small band gaps are obtained for FePSe₃ and NiPSe₃. This indicates that electronic correlation in these two compounds with partially filled $3d$ shells is quite important and must be taken into account. The band structures for FePSe₃ and NiPSe₃ using GGA+D2+U approximation using the on-site Hubbard parameter $U = 4\text{eV}$ are presented in Figure 4 and the obtained band gaps are reported in Table 3. With the improved description of electronic correlation, the band gaps of FePSe₃ and NiPSe₃ are obtained as 1.13 eV and 1.37 eV, respectively. These values are in good agreement with previous calculations in Ref. [17].

3.2 Magnetic Properties of NiPSe₃ monolayer

Among the three investigated magnetic states, the anti-ferromagnetic (AFM) with Neel ordering was predicted to be the most stable magnetic ground state for NiPSe₃ monolayer. This is also in qualitative agreement with Chittari *et al.*, [17]. The magnetic interactions for NiPSe₃ are evaluated using the ground-state energies of the four different magnetic configurations. The different spin configurations are Ferromagnetic (FM), AFM-Neel, AFM-zigzag and AFM-stripy ordered using $2 \times 1 \times 1$ supercell shown in Figures 2. The exchange interaction parameters between the Ni ions spins are extracted from the Heisenberg Hamiltonian in equations (2) while the magnetic energies are expressed explicitly in equations (3) and (4). The results of the nearest neighbour (NN) exchange interaction, J_1 , the next nearest neighbour (NNN) and third nearest neighbour (3NN) J_2

Table 2: The magnetic moments in Bohr magneton μ_B per Nickel atom, the three nearest neighbour exchange coupling strength J_i in meV for single layer NiPSe₃

Source	FM	NAFM	zAFM	sAFM	J_1	J_2	J_3
GGA	1.12	1.05	1.05	1.15	-17.46	-0.22	7.17
Theory[17]	0.54	0.94	0.12	0.99	127	-82.3	-67.6
GGA+U	1.30	1.24	1.23	1.29	-11.27	-0.28	4.70
Theory[17]	1.14	1.08	1.22	1.14	-3.11	1.04	18.2

and J_3 , respectively, obtained with GGA+D2 and GGA+D2+U are reported in Table 2. The average values of the magnetic moments at the Ni-atom at different magnetic configurations are also shown in Table 2 and compared with results from Ref. [17]. We find that the magnetic moment of Ni is similar in all magnetic configurations, and amount to $\sim 1.1\mu_B$ in GGA+D2 and $\sim 1.3\mu_B$ in GGA+D2+U. This is consistent with the idea that Ni is in a $3d^9$ configuration having approximately one hole in the d shell that causes a spin magnetic moment of $\sim 1\mu_B$ supplemented by an orbital magnetic moment. Among the exchange coupling constants, J_1 is largest in absolute magnitude and has negative sign which is indicative of the dominant antiferromagnetic coupling. The second largest coupling constant is J_3 ; its positive sign points toward the presence of some magnetic frustration, but the AFM ground state is still stabilized due to the dominating nearest-neighbor interaction. In a theory that neglects the Hubbard parameter U , the exchange coupling constants tend to be too large in absolute magnitude while the GGA+D2+U method gives more realistic values. Comparing to Ref.[17], their exchange coupling constants appear to be unrealistically large, in particular when U has been neglected.

3.3 Elastic Properties

It is well known that, in hexagonal crystals, three independent elastic constants are sufficient to entirely describe the behavior of the components of the elasticity tensor. Here, C_{11} , C_{12} and C_{66} (in Voigt notation) for 2D MPSe₃ under in-plane deformation are computed using the energy – strain approach. The stretching and shearing deformations were used to compute the elastic tensors C_{11} , C_{12} and C_{66} by a polynomial fit of the energy – strain relationships. The obtained values are collected in Table 3 for both the DFT and the DFT+U approach. The mechanical properties such as Young’s modulus (Y_s) and Poisson’s ratio (σ) are calculated using the computed elastic constants as expressed in eq.s (9) and (10), respectively.

$$Y_s = \frac{C_{11}^2 - C_{12}^2}{C_{11}} \quad (9)$$

$$\sigma = \frac{C_{11}}{C_{12}} \quad (10)$$

Young’s modulus gives a good insight about the stiffness of the materials. The stiffness is also an essential quantity which is required in order to avoid curling during the exfoliation process of 2D crystals.

Table 3: The energy gap E_g (eV), Debye temperature θ_D (K) the elastic constants C_{ij} (Nm^{-1}), *Young's modulus* Y_s (Nm^{-1}) and *Poisson's ratio* σ for MPSe₃ monolayers

System	Source	E_g	θ_D	C_{11}	C_{12}	C_{66}	Y_s	σ
CdPSe ₃	DFT	1.24	333.09	3.42	1.01	2.51	3.12	3.39
FePSe ₃	DFT	0.27	355.17	4.87	1.71	3.06	4.27	2.85
	Theory[17]	0.20	—	—	—	—	—	—
FePSe ₃	DFT+U	1.13	—	5.83	0.69	5.07	5.75	8.46
	Theory[17]	1.19	—	—	—	—	—	—
NiPSe ₃	DFT	0.59	375.55	4.94	1.05	4.20	4.71	4.71
	Theory[17]	0.59	—	—	—	—	—	—
NiPSe ₃	DFT+U	1.37	—	4.91	1.03	4.13	4.69	4.74
	Theory[17]	1.31	—	—	—	—	—	—

3.4 Lattice Dynamics

The possibility of 2D MPSe₃ monolayers being exfoliated from the bulk compounds depends on several factors some of which are the evaluation of the cleavage energy, their elastic properties and their dynamical stability. The dynamical stability of MPSe₃ monolayers were determined by calculating the phonon spectra within density functional perturbation theory (DFPT). A rhombic unit cell for the hexagonal crystal structures with two metal atoms in the non-magnetic state is used for the calculations. With 10 atoms in the unit cell, 30 phonon modes are obtained. The phonon dispersion along the high-symmetry directions of the hexagonal Brillouin zone with their respective phonon density of states (PDOS) are presented in Figs 5. The highest optical frequencies in all three materials are related to vibrations of the P–P structural unit, as indicated by the PDOS. These maximum optical frequencies are 311.89cm^{-1} , 287.04cm^{-1} and 310.88cm^{-1} for the CdPSe₃, FePSe₃, and NiPSe₃ monolayers, respectively. Moreover, there are optical modes of mixed character: In FePSe₃, and NiPSe₃, a pronounced maximum in the PDOS is due to mixed Fe – Se or Ni – Se vibrations around 240cm^{-1} and 200cm^{-1} . These frequency ranges are in agreement with the experimental observation of a Raman-active A_{1g} mode [29]. For the heavier Cd atom in CdPSe₃, the corresponding modes are observed at lower frequencies. In all three monolayers, there is a dense region of optical phonon bands in the range between 50 and 150cm^{-1} .

The absence of imaginary modes observed in the phonon dispersions of CdPSe₃ and NiPSe₃ is a strong indication that they are dynamically stable, they can thus be isolated experimentally as freestanding layers. The presence of a soft phonon mode (imaginary frequencies, shown as negative values in the plot) is observed in the hexagonal FePSe₃ monolayer around lowest acoustic phonon branches at the Brillouin zone center. This indicates that the FePSe₃ monolayer in this hexagonal phase is dynamically unstable. The acoustic modes are known to exhibit large group velocities, thereby contributing substantially to heat transport by virtue of their high dispersion. In contrast, the optical phonon modes contribute less to heat transport due to their small group velocities and weak dispersion. The maxima of the acoustic branches of the CdPSe₃, FePSe₃, and NiPSe₃ monolayers are around 66.84cm^{-1} , 91.84cm^{-1} , and 78.63cm^{-1} , re-

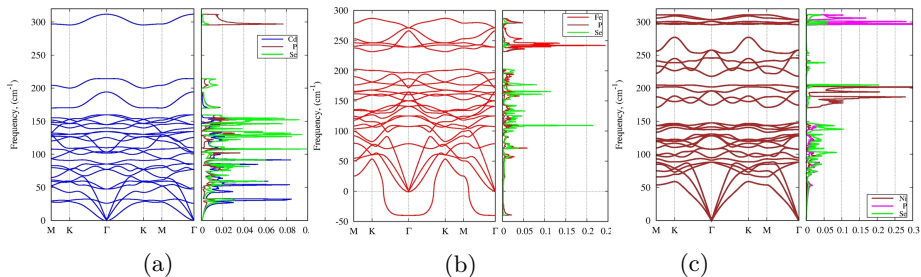


Figure 5: Phonon dispersion with respective phonon density of states for (a) CdPSe₃ (b) FePSe₃ (c) NiPSe₃ monolayers

spectively. Overlap between high-frequency acoustic modes and low-frequency optical modes exists in all three monolayers; this indicates the possibility of strong phonon–phonon scattering [41]. Typically, the thermal conductivity is often inherently restricted by anharmonic phonon-phonon scattering [41].

According to the phonon DOS presented alongside the phonon dispersions, considering the low frequency range up to 100 cm⁻¹, the major significant atomic contributions observed from (Cd, Fe)PSe₃ monolayers are M Cd, Fe and Se vibrations while from NiPSe₃ are from the P and Se. Therefore, the substitution at the M and Se sites, e.g. by species used for doping, can possibly change the carrier concentration while at the same time reducing the lattice thermal conductivity of the system.

3.5 Thermodynamic properties

The Debye temperature is a useful indicator for the range of temperatures in which a material can be successfully employed in a thermoelectric device. As an estimate of the Debye temperature θ_D we use the highest frequency of the normal mode vibrations ω_{\max} (Debye frequency),

$$\theta_D = \frac{\hbar\omega_{\max}}{k_B}, \quad (11)$$

where \hbar is the reduced Planck constant and k_B is the Boltzmann constant. The Debye temperature θ_D is an important parameter which defines the temperature above which all modes begin to be excited [42]. Moreover, it has a significant effect on heat transport. The Debye temperatures θ_D for the investigated systems are reported in Table 3.

Furthermore, the thermodynamic properties such as the internal energy, the Helmholtz free energy $F(T)$, the entropy $S(T)$, and the constant-volume heat capacity $C_V(T)$ were calculated using the phonon frequencies in the whole Brillouin zone within the harmonic approximation.

Fig. 6 shows the temperature dependence of the calculated internal energy, Helmholtz free energy, entropy, and constant-volume heat capacity. The unstable FePSe₃ monolayer has been excluded from the analysis. For the investigated systems, CdPSe₃ and NiPSe₃ monolayers, the vibrational entropy increases with increasing temperature, while the free energy decreases with increasing temperature. The entropy and constant-volume heat capacity in Figs 6c and 6d are zero at 0 K, in agreement with the third law of thermodynamics. The heat capacity

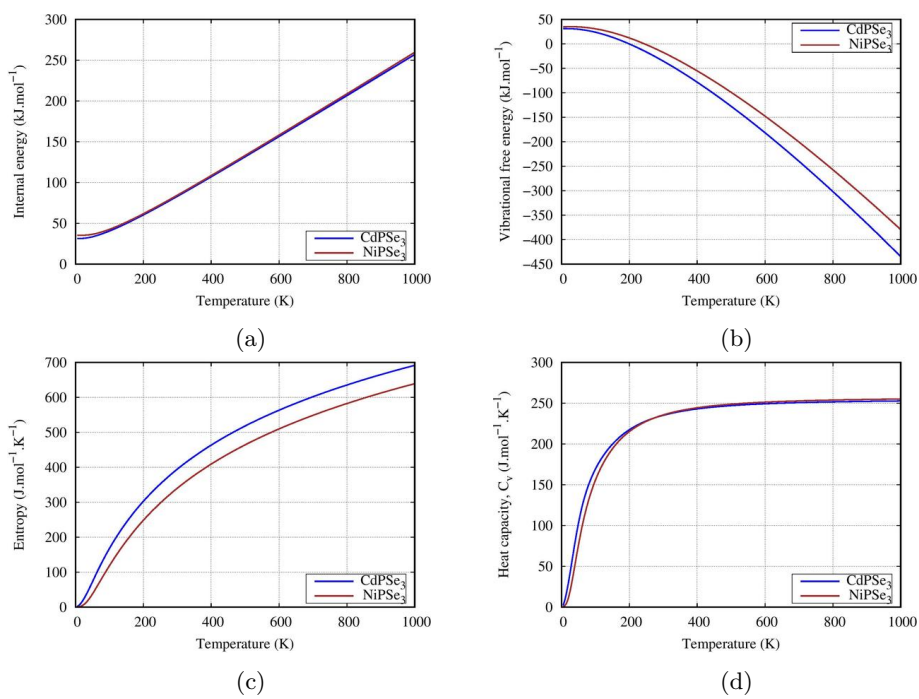


Figure 6: Temperature dependence of (a) internal energy (b) vibrational free energy (c) entropy (d) constant-volume heat capacity for CdPSe₃ and NiPSe₃ monolayers

approaches the Dulong–Petit classical limit of $250 \text{ J mol}^{-1}\text{K}^{-1}$ at high temperatures from 500 K upward. We note that for the AFM NiPSe₃ monolayer, excitations of spin waves will additionally contribute to the thermodynamic properties, in particular close to the Neel temperature.

3.6 Thermoelectric properties

As all the investigated materials are semiconductors, one can expect to find quite high Seebeck coefficients. When suitably doped, the monolayer could therefore show interesting thermoelectric properties. To assess this possibility, we discuss the thermoelectric figure of merit. The figure of merit ZT as given in eq. 5 can alternatively be written as eq. 12

$$zT = \frac{S^2\sigma T}{\kappa_{el} + \kappa_{ph}} = \frac{S^2\sigma T}{\kappa_{el}} \left(\frac{1}{1 + \kappa_{ph}/\kappa_{el}} \right) = \frac{(ZT)_{el}}{1 + \kappa_{ph}/\kappa_{el}} \quad (12)$$

where κ_{el} and κ_{ph} are the electronic and phononic contributions of the thermal conductivity respectively. $(ZT)_{el} = S^2\sigma T/\kappa_{el}$ is the *electronic* figure of merit. It can be understood as an upper bound to the total figure of merit and does not include the phononic contribution to the thermal conductivity.

While the Seebeck coefficient can be reasonably approximated just from the knowledge of the electronic band structure, the other two quantities entering into $(ZT)_{el}$, σ and κ_{el} , both depend on the electronic relaxation time τ . However, taking the ratio σ/κ_{el} , the effect of τ largely cancels out. Therefore it is possible to get a first estimate for the thermoelectric capabilities of a material from $(ZT)_{el}$ without requiring further input. The relaxation time τ in this present work is assumed to be isotropic and constant in all directions [43]. According to the BoltzTraP code [38], the transport properties of the materials is majorly dominated by the carriers in the narrow energy range near the Fermi level, while the relaxation time is assumed to be the same for all carriers in this range. The accuracy of this assumption has been validated, and proven to be a good approximation of the results of the thermoelectric properties [44, 45, 46]. Moreover, τ is kept as fixed parameter for the computation of electrical conductivity and electronic thermal conductivity since neither experimental values of τ nor related physical quantity is available.

The electrical conductivity σ as a function of relaxation time τ was computed for MPSe₃ within the temperature range of 0 - 600 K.

Based on DFT formalism we carried out calculations of the thermoelectric properties of CdPSe₃, FePSe₃ and NiPSe₃ for values of the chemical potential μ -0.411 Ry , -0.211 Ry and -0.526 Ry respectively. Moreover, the DFT+U calculations were carried out for FePSe₃ and NiPSe₃ at chemical potential μ -0.374 Ry and -0.507 Ry .

The electronic thermal conductivity, κ_{el} increase linearly with temperature for all the systems and this is an indication of continuous availability of charge carriers as temperature increases.

The Seebeck coefficients, S , defined as the thermoelectric parameter, which attest to the electronic structures within the Fermi levels show an increase from low temperature to room temperature from negative values to zero where it remain relatively constant in CdPSe₃. Meanwhile a steady increase with temperature is observed in NiPSe₃ but a gradual decrease with temperature is shown in FePSe₃.

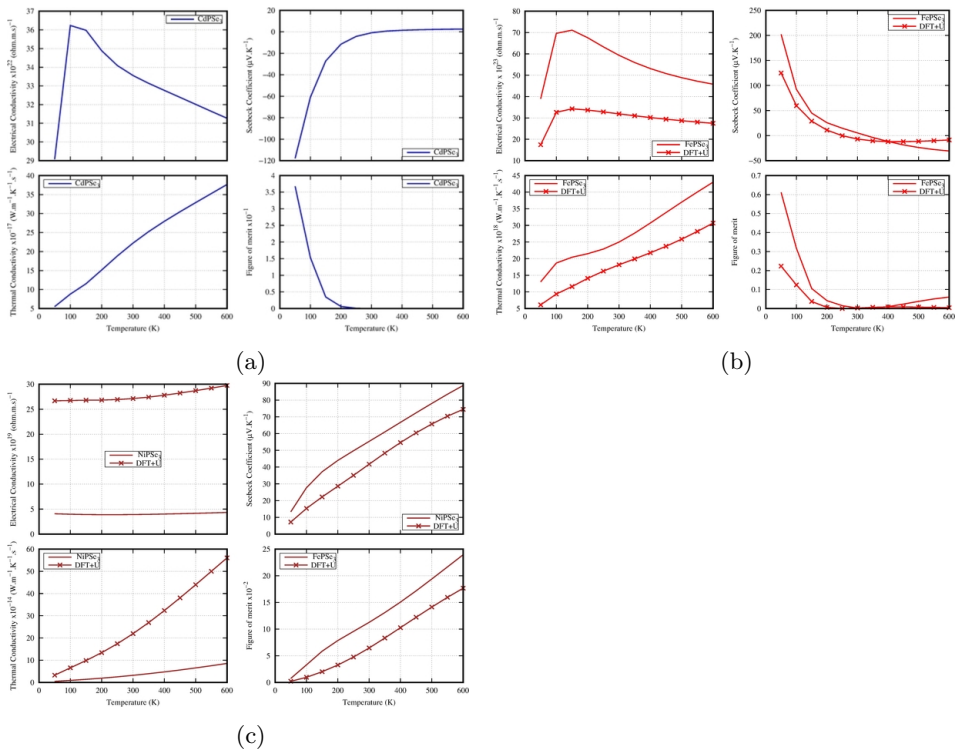


Figure 7: The computed electrical conductivity, seebeck coefficient, electronic thermal conductivity and electronic figure of merit for (a) CdPSe₃ (b) FePSe₃ (c) NiPSe₃ monolayers

Table 4: The carrier concentrations, n (cm^{-3}), seebeck coefficient, S (VK^{-1}), electrical conductivity, σ/τ ($\Omega^{-1}m^{-1}s^{-1}$) and electronic figure of merit ZT_{el} for single layer $MPSe_3$

Compd.	Source	Carrier	n (cm^{-3})	S	σ/τ	$(ZT)_{el}$
CdPSe ₃	DFT	hole	1.71×10^{15}	-0.94×10^{-4}	0.27×10^{24}	0.34
		electron	2.16×10^{15}	-0.13×10^{-3}	0.20×10^{24}	0.65
FePSe ₃	DFT	hole	2.56×10^{15}	1.65×10^{-4}	2.13×10^{24}	1.22
	DFT+U	hole	5.34×10^{15}	-1.27×10^{-4}	2.79×10^{24}	0.54
NiPSe ₃	DFT	hole	1.15×10^{15}	-8.98×10^{-4}	2.19×10^{14}	0.97
		electron	8.01×10^{13}	6.84×10^{-4}	8.71×10^{15}	1.03
	DFT+U	hole	7.52×10^{12}	8.42×10^{-4}	3.46×10^{13}	1.04
		electron	1.36×10^{12}	-2.09×10^{-4}	1.23×10^{19}	0.75

The electronic figure of merit, ZT_{el} gives good approximation of thermoelectric responsiveness of a material. These are reported jointly with other thermoelectric parameters in Figures 7. CdPSe₃ is observed to have maximum figure of merit of 0.37 at 100 K while the maximum figure of merits are observed to be respectively 0.6 and 0.25 at temperature 50 K for FePSe₃ using DFT and DFT+U approaches.

The maximum ZT values of singer layer $MPSe_3$ ($M = Cd, Fe, \text{ and } Ni$) and the corresponding carrier concentrations are depicted in Table 4.

The dependence of the figure of merit, ZT values of the 2D $MPSe_3$ ($M = Cd, Fe \text{ and } Ni$) on the carrier concentration and temperature is depicted in Figure 8. First, the optimal states of all p-type and n-type systems are forecasted to exhibit a ZT value in the range of 0.34 to 1.22 as revealed by the DFT and DFT+U approaches (see Table 4). As observed from Figure 8, the DFT approach predicts higher values of ZT when compared to DFT+U results. Moreover, FePSe₃ monolayer has p-type doping only. As revealed by DFT, the maxima ZT achieved for p-type doped CdPSe₃, FePSe₃ and NiPSe₃ at optimised carrier concentration are 0.34, 1.22 and 1.03 respectively. Meanwhile, the maxima observed for n doped CdPSe₃ and NiPSe₃ are 0.65 and 1.03 respectively. The DFT+U approach was applied for 2D FePSe₃ and NiPSe₃, this respectively predicts 0.54 and 1.04 for the p-type while the n-type ZT for 2D NiPSe₃ is 0.75. Lastly, It was clealy shown from 8 that the maxima ZT were achieved at low temperature of 50 K for CdPSe₃ and FePSe₃ monolayers while NiPSe₃ monolayer showed that the largest ZT at 100 K.

4 Conclusion

Using DFT and DFT+ U calculations, this work established that NiPSe₃ is an anti-ferromagnetic (AFM) semiconductor while CdPSe₃ and FePSe₃ are non magnetic semiconductors with indirect band gap of 1.37 eV, 1.24 eV and 1.13 eV respectively. DFPT calculation predicts that CdPSe₃ and NiPSe₃ are structurally and dynamically stable compound in the hexagonal structure while the negative frequencies observed along the brillouin zone in the phonon dispersion of FePSe₃ indicates structural instability in the hexagonal structure. Though, FePSe₃ monolayer is predicted to be unstable but it can still relax more and

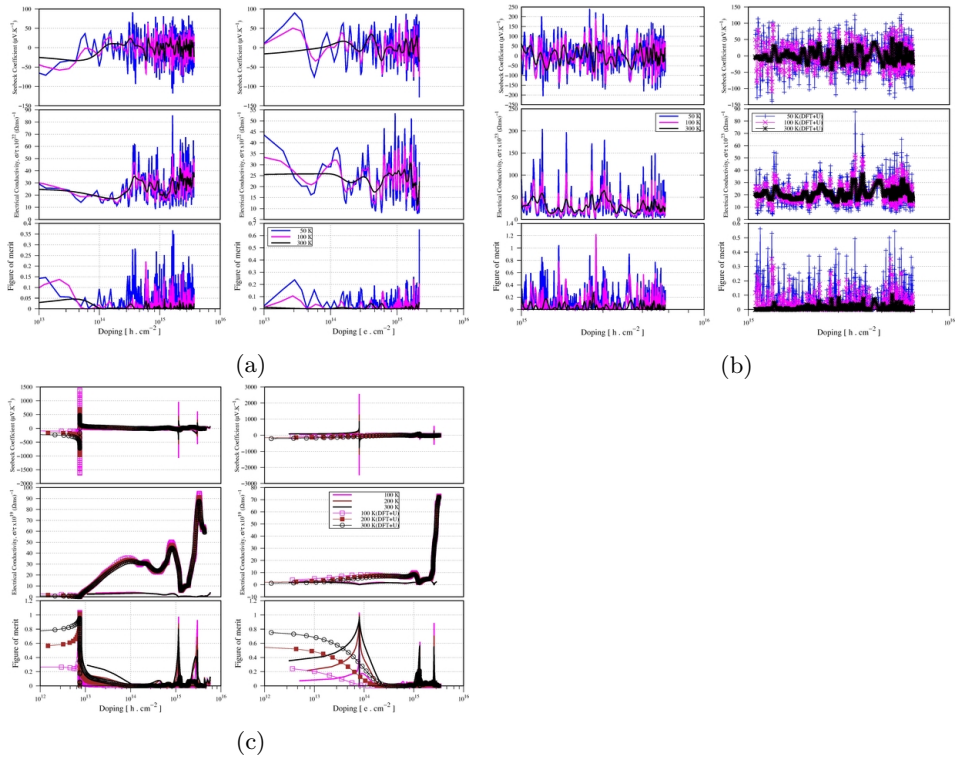


Figure 8: The computed electrical conductivity, seebeck coefficient, electronic thermal conductivity and electronic figure of merit for (a) CdPSe₃ (b) FePSe₃ (c) NiPSe₃ monolayers

become stable in other configuration, therefore the properties computed are suggestive and can serve as the basis for further investigation. In addition, the three investigated systems show good response to strain hence they can be said to be mechanically stable. The calculated thermoelectric properties show that p-doped FePSe₃ has highest electronic figure of merit at low temperature of 50 K as revealed in Table 4 .

5 Acknowledgement

The work has been performed under the Project HPC-EUROPA3 (INFRAIA-2016-1-730897), with the support of the EC Research Innovation Action under the H2020 Programme; in particular, A.A. Musari acknowledges the Hawk HPC provided by University of Stuttgart. AAM also appreciates the support of Faculty of Physics, University of Duisburg-Essen Germany throughout his stay.

References

- [1] K. S. Novoselov, A. K. Geim, S. V. Morozov, D. Jiang, Y. Zhang, S. V. Dubonos, I. V. Grigorieva and A. A. Firsov, Electric field effect in atomically thin carbon films. *Science*, 306, (2004) 666–669.
- [2] K. S. Novoselov, D. Jiang, F. Schedin, T. J. Booth, V. V. Khotkevich, S. V. Morozov and A. K. Geim, Two-dimensional atomic crystals. *Proceedings of the National Academy of Sciences*, 102, (2005) 10451–10453.
- [3] K. F. Mak, C. Lee, J. Hone, J. Shan and T. F. Heinz, Atomically thin MoS₂: A new direct-gap semiconductor, *Phys. Rev. Lett.*, 105, (2010) 136805.
- [4] S. Cahangirov, M. Topsakal, E. AktuÅrk, H. S Sahin and S. Ciraci, Two- and one-dimensional honeycomb structures of silicon and germanium. *Phys. Rev. Lett.*, 102, (2009) 236804.
- [5] C. R. Dean, A. F. Young, I. Meric, C. Lee, L. Wang, S. Sorgenfrei, K. Watanabe, T. Taniguchi, P. Kim, K. L. Shepard and J. Hone, Boron nitride substrates for high-quality graphene electronics. *Nature nanotechnology*, 5, (2010) 722–726.
- [6] Q. H. Wang, K. Kalantar-Zadeh, A. Kis, J. N. Coleman and M. S. Strano, Electronics and optoelectronics of two-dimensional transition metal dichalcogenides. *Nature nanotechnology* 7, (2012) 699–712.
- [7] W. Yang, G. Chen, Z. Shi, C. C. Liu, L. Zhang, G. Xie, ... and G. Zhang. Epitaxial growth of single-domain graphene on hexagonal boron nitride. *Nature materials*, 12(9), (2013) 792-797.
- [8] Z. Liu, L. Ma, G. Shi, W. Zhou, Y. Gong, S. Lei, ... and P. M. Ajayan. In-plane heterostructures of graphene and hexagonal boron nitride with controlled domain sizes. *Nature nanotechnology*, 8(2), (2013) 119-124.
- [9] S. Dai, Z. Fei, Q. Ma, A. S. Rodin, M. Wagner, A. S. McLeod, ... and D. N. Basov. Tunable phonon polaritons in atomically thin van der Waals crystals of boron nitride. *Science*, 343(6175), (2014) 1125-1129.

- [10] G. Cassabois, P. Valvin and B. Gil. Hexagonal boron nitride is an indirect bandgap semiconductor. *Nature photonics*, 10(4), (2016) 262-266.
- [11] V. Nicolosi, M. Chhowalla, M. G. Kanatzidis, M. S. Strano, and J.N. Coleman. Liquid exfoliation of layered materials. *Science*, 340 (2013) (6139).
- [12] Z. Ye, T. Cao, K. O'brien, H. Zhu, X. Yin, Y. Wang, ... and X. Zhang. Probing excitonic dark states in single-layer tungsten disulphide. *Nature*, 513(7517), (2014) 214-218.
- [13] S. -Y. Xu, I. Belopolski, N. Alidoust, M. Neupane, G. Bian, C. Zhang, ... and M. Z. Hasan, Discovery of a Weyl fermion semimetal and topological Fermi arcs. *Science*, 349 (6248), (2015) 613-617.
- [14] W. Xu, W. Liu, J. F. Schmidt, W. Zhao, X. Lu, T. Raab, ... and Q. Xiong. Correlated fluorescence blinking in two-dimensional semiconductor heterostructures. *Nature*, 541 (7635), (2017) 62-67.
- [15] D. Ovchinnikov, F. Gargiulo, A. Allain, D. J. Pasquier, D. Dumcenco, C. H. Ho, ... and A. Kis. Disorder engineering and conductivity dome in ReS₂ with electrolyte gating. *Nature communications*, 7(1), (2016) 1-7.
- [16] W. B. Zhang, Q. Qu, P. Zhu, and C. H. Lam, Robust intrinsic ferromagnetism and half semiconductivity in stable two-dimensional single-layer chromium trihalides. *Journal of Materials Chemistry C*, 3(48), (2015) 12457-12468.
- [17] B. L. Chittari, Y. Park, D. Lee, M. Han, A. H. MacDonald, E. Hwang, and J. Jung. Electronic and magnetic properties of single-layer MPX₃ metal phosphorous trichalcogenides. *Physical Review B*, 94(18), (2016) 184428.
- [18] J. Yang, Y. Zhou, Q. Guo, Y. Dedkov, and E. Voloshina. Electronic, magnetic and optical properties of MnPX₃ (X= S, Se) monolayers with and without chalcogen defects: a first-principles study. *Rsc Advances*, 10(2), (2020) 851-864.
- [19] F. Wang, T. A. Shifa, P. Yu, P. He, Y. Liu, F. Wang ... and J. He. New frontiers on van der Waals layered metal phosphorous trichalcogenides. *Advanced Functional Materials*, 28(37), (2018) 1802151.
- [20] N. Sivadas, M.W. Daniels, R. H. Swendsen, S. Okamoto and D. Xiao, Magnetic ground state of semiconducting transition-metal trichalcogenide monolayers *Phys. Rev. B: Condens. Matter. Phys.*, 91, (2015) 235425.
- [21] J. Liu, Q. Sun, Y. Kawazoe and P. Jena. Exfoliating biocompatible ferromagnetic Cr-trihalide monolayers. *Physical Chemistry Chemical Physics*, 18(13), (2016) 8777-8784.
- [22] S. Sarkar and P. Kratzer. Electronic correlation, magnetic structure, and magnetotransport in few-layer CrI₃, *Phys. Rev. Mater.* 4 (2020), 104006.
- [23] S. Sarkar and P. Kratzer. Magnetic exchange interactions in bilayer CrX₃ (X = Cl, Br, and I): A critical assessment of the DFT + U approach. *Physical Review B*, 103 (22), (2021) 224421.

- [24] C. Gong, L. Li, Z. Li, H. Ji, A. Stern, Y. Xia, ... and Z. Q. Qiu, Discovery of intrinsic ferromagnetism in two-dimensional van der Waals crystals. *Nature*, 546(7657), (2017) 265-269.
- [25] S. Kang, S. Kang, and J. Yu Effect of Coulomb Interactions on the Electronic and Magnetic Properties of Two-Dimensional CrSiTe₃ and CrGeTe₃ Materials. *Journal of Electronic Materials*, 48(3), (2019) 1441-1445.
- [26] X. Li, T. Cao, Q. Niu, J. Shi and J. Feng. Coupling the valley degree of freedom to antiferromagnetic order. *Proceedings of the National Academy of Sciences*, 110 (10), (2013) 3738-3742.
- [27] X. Li, X. Wu and J. Yang. Half-metallicity in MnPSe₃ exfoliated nanosheet with carrier doping. *Journal of the American Chemical Society*, 136 (31), (2014) 11065-11069.
- [28] P. Sen and R. K. Chouhan Electronic structure of MPX₃ trichalcogenide monolayers in density functional theory: a case study with four compounds (M= Mn, Fe; X= S, Se). *Electronic Structure*, 2(2), (2020) 025003.
- [29] Ke-zhao Du, Xing-zhi Wang, Yang Liu, Peng Hu, M. Iqbal Bakti Utama, Chee Kwan Gan, Qihua Xiong and Christian Kloc, Weak van der Waals Stacking, Wide-Range Band Gap, and Raman Study on Ultrathin Layers of Metal Phosphorus trichalcogenides, *ACS Nano* 10 (2016), 1738.
- [30] P. Giannozzi, S. Baroni, N. Bonini, M. Calandra, R. Car, C. Cavazzoni, ... and A. Dal Corso (2009). QUANTUM ESPRESSO: a modular and open-source software project for quantum simulations of materials. *Journal of physics: Condensed matter*, 21(39), 395502.
- [31] J. P. Perdew, K. Burke and M. Ernzerhof. Generalized gradient approximation made simple. *Physical review letters*, 77(18), (1996) 3865.
- [32] S. Grimme Semiempirical GGA-type density functional constructed with a long-range dispersion correction. *Journal of computational chemistry*, 27(15), (2006) 1787-1799.
- [33] V. Barone, M. Casarin, D. Forrer, M. Pavone, M. Sami and A. Vittadini. Role and effective treatment of dispersive forces in materials: Polyethylene and graphite crystals as test cases. *Journal of computational chemistry*, 30(6), (2009) 934-939.
- [34] M. Cococcioni and S. De Gironcoli. Linear response approach to the calculation of the effective interaction parameters in the LDA + U method. *Physical Review B*, 71 (3), (2005) 035105.
- [35] H. J. Monkhorst and J. D. Pack (1976). Special points for Brillouin-zone integrations. *Physical review B*, 13(12), 5188.
- [36] A. Dal Corso and S. de Gironcoli, Density-functional perturbation theory for lattice dynamics with ultrasoft pseudo-potentials, *Phys. Rev. B*, 62, (2000) 273.
- [37] P. Giannozzi and S. Baroni S., Density-Functional Perturbation Theory. In: Yip S. (eds) *Handbook of Materials Modeling*. Springer, Dordrecht (2005).

- [38] G. K. Madsen and D. J. Singh. BoltzTraP. A code for calculating band-structure dependent quantities. *Computer Physics Communications*, 175(1), (2006) 67-71.
- [39] A. Wiedenmann, J. Rossat-Mignod, A. Louisy, R. Brec and J. Rouxel Neutron diffraction study of the layered compounds MnPSe_3 and FePSe_3 . *Solid State Communications*, 40 (12), (1981) 1067-1072.
- [40] W. Klingen, G. Eulenberger and H. Hahn. About the crystal structures of $\text{Fe}_2\text{P}_2\text{Se}_6$ and $\text{Fe}_2\text{P}_2\text{S}_6$. *Journal of Inorganic and General Chemistry*, 401 (1), (1973) 97-112.
- [41] V. K. Gudelli, V. Kanchana, G. Vaitheeswaran, D. J. Singh, A. Svane, N. E. Christensen and S. D. Mahanti Electronic structure, transport, and phonons of SrAgChF ($\text{Ch} = \text{S, Se, Te}$): Bulk superlattice thermoelectrics. *Physical Review B*, 92(4), (2015) 045206.
- [42] T. Nakashima and Y. Umakoshi, Anisotropy of electrical resistivity and thermal expansion of single-crystal Ti_5Si_3 , *Philosophical Magazine Letters*, 66(6), (1992) 317–321.
- [43] W. W. Schulz, P. B. Allen, and N. Trivedi, Hall coefficient of cubic metals. *Physical Review B*, 45(19), (1992) 10886.
- [44] R. Chmielowski, D. Pér é, C. Bera, I. Opahle, W. Xie, S. Jacob, ... and G. Dennler, Theoretical and experimental investigations of the thermoelectric properties of Bi_2S_3 . *Journal of Applied Physics*, 117(12), (2015) 125103.
- [45] H. Shi, D. Parker, M.-H. Du, and D. J. Singh, Connecting thermoelectric performance and topological-insulator behavior: Bi_2Te_3 and $\text{Bi}_2\text{Te}_2\text{Se}$ from first principles. *Physical Review Applied*, 3(1), (2015) 014004.
- [46] G. Dennler, R. Chmielowski, S. Jacob, F. Capet, P. Roussel, S. Zastrow ... and G. K. Madsen, Are binary copper sulfides/selenides really new and promising thermoelectric materials?. *Advanced Energy Materials*, 4(9), (2014) 1301581.
- [47] A. H. Reshak, S. A. Khan and S. Auluck. Thermoelectric properties of a single graphene sheet and its derivatives. *Journal of Materials Chemistry C*, 2(13), (2014) 2346-2352.
- [48] K. Yang, S. Cahangirov, A. Cantarero, A. Rubio and R. D'Agosta. Thermoelectric properties of atomically thin silicene and germanene nanostructures. *Physical Review B*, 89(12), (2014) 125403.

First Principle Calculations of Structural, Electronic, Magnetic, Mechanical and Thermodynamic Properties of XCrGe (X = Hf and Zr) Half-Heusler compounds

Structural, electronic, magnetic and thermodynamic properties of XCrGe (X = Hf and Cr) half-Heusler alloys have been studied using first principle Density Functional Theory (DFT) with the state of the art full-potential linearized augmented plane wave (FP-LAPW) method. Both compounds were observed to be ferromagnetic and half-metallic in nature with a small band gap in their spin up (majority) channels. The Slater-Pauling rule was employed to predict the total magnetic moment of $4\mu_B$ which agree with the values obtained in the calculation. Their mechanical properties show that they are mechanically stable and ductile in nature. The directional dependences of Young's modulus, shear modulus, Poisson's ratio and linear compressibility (in the xy, xz and yz planes) were presented. This theoretical investigation suggests that the two materials have the potential of being used as spintronics devices. Keywords: Half-Heusler, first-principles, electronic structure, magnetism, mechanical behaviours

THE ELECTRONIC, STRUCTURAL AND OPTICAL PROPERTIES OF BARIUM PEROVSKITE COMPOUND

In this research, first-principle density functional theory calculation was used to determine the structural, electronic and optical properties of ternary perovskite compound (BaTiS₃). Bandgaps of 1.61 eV. This band gap values shows that BaTiS₃ is ideal for photovoltaic applications. The high absorption spectra of $7 \times 10^8 \text{ m}^{-1}$, low reflectivity of 0.7, refractive index of 8.2 and dielectric function of 78 were obtained. This suggests that the compound is a good application in light harvesting for energy storage.

Optical properties of Zn doped AgInSe₂ Chalcopyrite semiconductor.

AgInSe₂ chalcopyrite has been predicted to be promising materials in solar cell application. Extensive research has been carried out both experimentally and from first principles on the optical behaviour of the alloy in various configurations. In this work we present results for the optical properties of Zn doped AgInSe₂ at the 4a site occupied by Ag. The measurement of the transmission and reflection coefficients is carried out along with other optical parameters like the dielectric constants and absorption coefficient. The alloy exhibits a direct bandgap of 1.42 eV. Details of other results will be reported consequently.

Study of the electronic and optical properties of antiperovskite Mg_3XN ($\text{X}=\text{P}, \text{As}, \text{Sb}, \text{Bi}$): The GW/BSE approach

Antiperovskites are materials that have interesting properties and several applications. Unlike their perovskite counterparts, antiperovskites have not received much attention. Here, we study the electronic and optical properties of Mg_3XN ($\text{X}=\text{P}, \text{As}, \text{Sb}, \text{Bi}$) antiperovskites using the GW/BSE approach. The quasiparticle bandstructures of these materials were calculated using the one-shot GW (G0W0) and self-consistent GW (evGW). The G0W0 and evGW band gaps are in the energy range 1.37-2.33 eV and 1.52 -2.60 eV, respectively. Mg_3BiN has the lowest energy gap (indirect) value of 1.37eV, while Mg_3PN has the highest gap (direct) of 2.33eV. The inclusion of spin-orbit coupling (SOC) decreased the G0W0 gap for each material. Excitonic effect was accounted for by solving the Bethe Salpeter Equation (BSE) and different optical properties of the materials were calculated.

Understanding the role of oxygen Vacancies in the stability of ZnO(0001)-(1 × 3) surface reconstructions: a DFT study

The atomic-scale explanation of ZnO surface reconstructions is relevant to strengthen its use in technological applications and to conduct experimental efforts in improving growth procedures. Several surface reconstructions have been observed for both ZnO polar surfaces -the (0001) and (000 $\bar{1}$), which correspond to Zn and O terminations-. The experimental evidence for the (0001) surface reconstructions provides insight into the stabilization mechanisms vital for surface processes. In this work, the stability between the previously reported reconstructions (2 × 2), (4 × 4) pit, and (4 × 4) pit + Zn, against the (1 × 3) reconstruction found experimentally, is explored. The initially proposed Zn-vacancy model is not favorable in any range of oxygen chemical potential. Nevertheless, we report two stable reconstructions associated with O vacancies in the oxygen-poor limit. Models with single and double oxygen vacancies are candidates to match the (1 × 3) reconstruction. We present theoretical Tersoff–Hamann scanning tunneling microscopy images for both models and compare them with the experimental atomic force microscopy images. The striped pattern formed of single and double Zn rows -in the [2-1-10] direction-obtained from the two oxygen vacancy model is consistent with the experimental measurements. and (000 $\bar{1}$), which correspond to the Zn and O terminations. The experimental evidence for the (0001) surface reconstructions provides insight into the stabilization mechanisms vital for surface processes. This work explores the stability between the previously reported reconstructions (2 × 2), (4 × 4) pit, and (4 × 4) pit + Zn, against the (1 × 3) reconstruction found experimentally. It is found that the original Zn-vacancy model is not favorable in any range of oxygen chemical potential. We report two stable reconstructions for the oxygen-poor limit associated with O vacancies. Models with one and two oxygen vacancies arise as candidates to explain the (1 × 3) reconstruction. We present theoretical Tersoff–Hamann scanning tunneling microscopy images for both reconstructions and compare them with the experimental atomic force microscopy images. The striped pattern composed of single and double Zn rows, obtained from the two oxygen vacancy model, is consistent with the experimental measurements. The density of states of the stable models depicts metallic character, where the typical sp³ bulk hybridization is preserved in the upper layers. Charge density plots confirm the formation of Zn atomic wires in the [1000] direction.

Adsorption of noxious H₂S and HF Gases on 2D Penta-PdAs₂ Semiconductor as Gas Sensor : A DFT Study

As gas sensing of noxious gases specifically, H₂S and HF, have significant research interest for different applications in environments as well as in the human healthcare sector. Here the adsorption and gas sensing properties of monolayer penta-PdAs₂ to two kind of pollutant H₂S and HF gases have been investigated by means of density functional theory (DFT). The obtained results of gas adsorbed sheet, indicated that the electronics properties of penta-PdAs₂ are slightly affected by the pollutants gases (H₂S and HF). The found physisorption adsorption energy of H₂S (HF) gas molecules is -0.49 (-0.40) eV with the interesting recovery time of 2.5 μ s (0.36 μ s), revealed that both gases strongly adsorbed on penta-PdAs₂ sheet. In H₂S (HF) gas adsorbed systems, the charge transfer is -0.018 e (-0.020 e), indicated that the electrons are going to H₂S (HF) molecules from the PdAs₂ sheet. Simultaneously, the electronic transport (IV characteristics) and sensitivity of H₂S and HF were also investigated under non-equilibrium green's function (NEGF). Interesting results have been examined and will be put forward during this poster presentation as prototype for these results. Finally, our novel findings of H₂S and HF gas sensing on PdAs₂ monolayer might provide guidance in the designing of better sensing device at the nano-scale

Topological excitonic transition in organic polymers: singlet fission and negatively dispersing excitons

Topological phases like topological superconductors or Chern insulators have several potential applications in physics, ranging from quantum computing to the development of photonic crystals with protected transport properties. While many examples of materials with topological single particle states have been discovered, few examples of excitonic topological transitions have been clearly demonstrated. Here, by using state-of-the-art manybody perturbation theory techniques, we show that the topological Z_2 phase transition occurring in the single particle spectrum of the recently synthesized ethynylene-bridged polyacene polymers is accompanied by a topological excitonic phase transition. The band inversion in the non-trivial phase yields real-space exciton wave functions in which electrons and holes exchange orbital characters with respect to the trivial phase. The topological excitonic phase transition results in a broad tunability of the energy difference between singlet and triplet excitons, opening appealing perspectives for the occurrence of singlet fission. Finally, the flatness of the single-particle electronic structure in the topological non trivial phase leads to negatively dispersing triplet excitons in a large portion of the Brillouin zone. The authors acknowledge support from the ANR project ACCEPT (Contract No. 195608.). This work was granted access to the HPC resources of Jean-Zay (IDRIS) under the allocation 2021-A0100912417 made by GENCI.

$\text{Cs}_2\text{NaGaBr}_6$: A New Lead-Free Halide Double Perovskite with DirectBand Gap

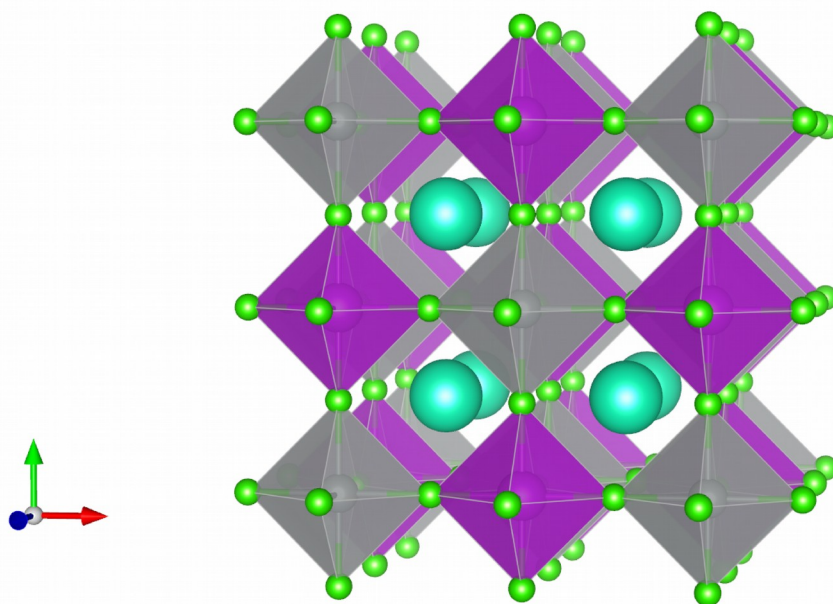
Haleema Khalil^a, Bin Amin^a, Fida Rehman^b, M. Shafiq^b and Yasir Saeed^b

^aDepartment of Physics, Hazara University, Mansehra, Pakistan

^bDepartment of Physics, Abbottabad University of Science and Technology, Havelian, Abbottabad, KPK, Pakistan

ABSTRACT

The double perovskites $\text{Cs}_2\text{NaGaBr}_6$ has been investigated using all-electron full-potential linearized augmented plane wave (FP-LAPW+lo) method within the frame work of the density functional theory. In addition to this, we employed Modified Back-Johnson bandgap correction (MBJ) in order to obtained close value of gap with respect to the experimental value. Our obtained bandgap is 1.762 eV with spin orbit coupling including MBJ. $\text{Cs}_2\text{NaGaBr}_6$ has direct bandgap at Γ -point which is similar to parent Organic-inorganic perovskite (MAPI) $\text{CH}_3\text{NH}_3\text{PbI}_3$ ($E_g=1.6$ eV) . Density of states shows that Br is major contributor near Fermi level with Ga specifically in CBM. We have calculated optical spectra to study absorption in $\text{Cs}_2\text{NaGaBr}_6$. We have calculated phonon band structure and found positive frequencies, which shows the stability. Stable, direct bandgap and value of gap close to MAPI makes $\text{Cs}_2\text{NaGaBr}_6$ a great competitor in Pb-free hybrid perovskites solar cell word.



Lead free double-perovskites based on thallium for thermoelectric and photovoltaic applications: A first-principle study of structural, optoelectronic and thermoelectric properties

Energy consumption rate is increasing tremendously with each passing day since last fifty years because of speedy industrial growth and population increase all over the world. The reliance on traditional fossil fuel power generation methods is causing a severe energy deficit. Therefore, to address this serious issue, the research in exploration of innovative materials for alternative cleaner and environment friendly power generation methods has attained much attention. Thermoelectric and photovoltaic materials have appeared as potential candidates in this scenario for producing power from wasted heat during conventional fossil fuel methods and from sun light available freely on earth respectively. In this work, the structural, electronic, optical and thermoelectric properties of double-perovskites $\text{Cs}_2\text{AgTlY}_6$ ($\text{Y}=\text{Br}, \text{Cl}$) have been studied using density functional theory. The calculated structural and electronic parameters fairly agree with reported experimental/theoretical findings. The direct band gaps, structural stability, thermal stability, significant absorption coefficients in visible range, large Seebeck coefficients and figure of merit (close to unity) of these lead-free thallium-silver based halide double-perovskites suggest that these compounds may play vital role in various optoelectronic and thermoelectric device applications.

Structural Vibrational, thermophysical and Electronic properties of $L1_0$ FePt and FePd

*B. P. Thacker**, *R. N. Kharatmol**, *N. Y. Pandya**, *Adwait Mevada⁺*, *P. N. Gajjar[#]*

** Parul University, P. O. Limda, Ta. Waghodia, Vadodara, 391 760, Gujarat, India*

⁺President Science College, Ghatlodia, Ahmedabad, 380 061, Gujarat, India

[#]Department of Physics, University School of Sciences, Gujarat University, Ahmedabad, 380009, Gujarat, India

Corresponding author: bhavik.thacker18410@paruluniversity.ac.in,

niravbhai.pandya12730@paruluniversity.ac.in,

Abstract:

An extensive first-principles calculation of the structural, vibrational and electronic properties of $L1_0$ FePt and FePd alloy is studied using plane-wave pseudopotential density functional theory (DFT). PAW type pseudopotential with the exchange correlation of Perdew-Burke-Ernzerhof (PBE) are used for the present computations. Our computed equilibrium lattice constants are in good agreement with the reported results. Phonon dispersions and phonon density of states of $L1_0$ FePt and FePd exhibit dynamically stable phase along the high symmetry directions of the Brillouin zone. Further, the electronic band structure along with the total and projected electronic density of states, electronic charge density and Fermi surfaces of $L1_0$ FePt and FePd are also studied. Various thermophysical properties, namely Room temperature thermal equation of states, Coefficient of thermal expansion at different temperatures, isothermal bulk modulus at different temperatures, Specific heats as a function of temperature, Temperature dependence of Debye temperature, Grüneisen parameter as a function of temperature are investigated using methodology as implemented in quasi-harmonic Debye model. Conclusions based on the phonon dispersion curves, phonon density of states, electronic band structure along with the total and projected electronic density of states, electronic charge density, Fermi surface and thermophysical properties are outlined.

Keywords: $L1_0$ FePt and FePd, Invar, DFT, Phonon dispersion curve, Phonon density of states, Electronic band structure, Electronic charge density, Fermi Surface, Thermophysical properties.

Excitons in MoSi₂Z₄ Family of 2D materials

Two-dimensional (2D) materials are at the forefront of research due to their promising electronic and optical properties. Among them, the newly added 2D synthetic MoSi₂Z₄ family is particularly important due to their exciting optoelectronic properties. However, the photo-physical properties of this family are yet to be examined. Here, we investigate the quasiparticle energies, optical absorption, exciton (bound electron-hole pair) properties, and carrier dynamics from the first principle calculation. Our study predicts that the excitons exist below the quasiparticle band gap in this family. The presence of spin-orbit coupling results in two excitonic peaks within the gap, which are the characteristic features of this family. The effect of charge carriers injection on the excitonic properties is studied by applying a strong pump pulse of 100 fs duration. When the dynamics of the charge carriers are taken into account, screening changes with the time evolution. This additional screening channel brings in exciton binding energy and bandgap variation, resulting in the renormalization of the bandgap and exciton energy. We observe both red and blue shifts of exciton energy in this material as a function of carrier density.